LOW-SPEED INVESTIGATION OF A
DOUBLE WEDGE AIRFOIL
WITH LEADING-EDGE SLAT

Thesis by
Richard Earl Wallace

In Partial Fulfillment of the Requirements
for the Degree of Aeronautical Engineer

California Institute of Technology
Pasadena, California
June, 1952

The author wishes to express his appreciation to the GALCIT wind tunnel staff for their assistance in conducting the tests and to his wife for her help in preparing the manuscript.

SUMMARY

A two-dimensional investigation was undertaken in the California Institute of Technology Merrill Wind Tunnel to determine the effectiveness of using a 15% slat on a 10% double wedge airfoil. The investigation was conducted in three phases: force polars, pressure tests, and tuft pattern studies. All phases were conducted at a dynamic pressure of 40 lb/ft^2, equivalent to a Reynolds number of 0.78×10^6.

The high lift characteristics of the double wedge airfoil with the slat were found to be aerodynamically superior to those of the basic wedge section and the wedge equipped with a plain nose flap. Extension of the leading edge slat caused increases in maximum lift coefficients and in the angle of attack required for maximum lift. The following increments were measured.

Config.	Basic Section	7-0	7-10	7-20	7-25	7-30	7-35	5_s-35
$C_{l_{max}}$	0.710	0.775	0.910	1.128	1.236	1.274	1.306	1.115
C_d	0.110	0.155	0.100	0.116	0.125	0.140	0.204	0.135
$\Delta C_{l_{max}}$	0	0.065	0.135	0.418	0.526	0.564	0.596	0.405
ΔC_d	0	0.045	-0.010	0.006	0.015	0.030	0.194	0.025
α_u	10°	14°	13°	16°	18°	20°	24°	19°

The nose deflection produced larger $C_{l_{max}}$ increments than the slot variations below nose angles of 25°, but for 25° and larger angles the slot variations caused the major improvements in $C_{l_{max}}$. The slot prevented occurrence of buffeting caused by upper surface intermittent or oscillatory separation

experienced with the plain nose flap.

In all of the cases tested with the slat extended, the stall was more gradual than for the basic section. The stall for the optimum slot conditions was the result of trailing edge separation moving forward over the upper surface of the airfoil.

TABLE OF CONTENTS

INDEX OF FIGURES

SYMBOLS

The term "main section of the airfoil" is herein considered to mean that part of the airfoil section excluding the slat. The aerodynamic coefficients and other symbols used are as follows:

a	Slat angle of rotation from the chord line (deg.)
b	Slat translation in half per cent chord units from the basic airfoil position (See fig. 2)
g	Slot gap in per cent of chord
c	Model chord with the slat retracted
S	Model projected area with the slat retracted
l	Model lift uncorrected for blocking
d	Model drag uncorrected for blocking
$m_{c/2}$	Model pitching moment about the 50% chord point, uncorrected for blocking
$m_{c/4}$	Model pitching moment about the quarter-chord point, uncorrected for blocking
q	Tunnel dynamic pressure ($\rho V^2/2$)
ρ	Tunnel air mass density
V	Tunnel air velocity, uncorrected for blocking
α_u	Model angle of attack measured from the airfoil chord line, uncorrected for blocking (degrees)
C_l	Section lift coefficient (l/qS)
$C_{l_{max}}$	Maximum uncorrected section lift coefficient
C_d	Section drag coefficient, uncorrected for blocking (d/qS)
$C_{m_{c/2}}$	Mid-chord section pitching moment coefficient ($m_{c/2} \div qSc$)
$C_{m_{c/4}}$	Quarter-chord section pitching moment coefficient ($m_{c/4} \div qSc$)
R.N.	Reynolds number

I-INTRODUCTION

Thin symmetrical supersonic airfoils with sharp leading and trailing edges are designed with flight at supersonic speeds as the paramount objective and their operation in the subsonic realm of flight comes as a secondary concern. However, safe operation of aircraft equipped with such airfoil sections at the low speeds required for landing and take-off necessitates methods for increasing their characteristically low maximum lift and reducing the large profile drag at these maximum lift coefficients. Previous investigations have involved various means of achieving these more desirable results and the most promising has proved to be the nose flap with its effective increase in camber. Nose flaps have shown promise in both reducing the drag at the maximum lift conditions and achieving higher maximum values of lift. References 1 and 2 describe a series of investigations conducted by the NACA Ames Aeronautical Laboratory at Moffett Field, California to determine the aerodynamic properties of a thin modified double wedge airfoil equipped with a nose flap and a simulated split flap. Reference 3 deals more specifically with their findings on the stalling of the airfoil and nose flap.

It was on the basis of these NACA reports that this investigation was prompted to find the effectiveness of slotting the nose flap in such a manner that it would act more as a slotted nose flap or "slat", as it will be referred to herein. In so doing, the favorable pressure differential between the upper and lower surfaces was to be utilized to add kinetic energy to the boundary layer on the suction side of the airfoil and delay the flow separation downstream from the juncture of the slat and the main body section. Also, since the flow over a sharp-edged nose flap is characterized by separation immediately behind the leading edge caused by the very high flow accelerations required to negotiate the sharp nose, additions of kinetic energy downstream from the separation could conceivably cause earlier flow reattachment than would otherwise be possible. Although the more artificial means of energy addition such as blowing or removing the boundary layer by suction could be performed, the utilization of the favorable pressure differential is more dependable and trouble free in the practical sense.

To achieve the desired results, the slat juncture with the main section of the airfoil was shaped as a favorable converging channel. Then, with the slat as an external element, it was free to be moved away from the body and form a channel through which the air might pass and by the induced acceleration convert the pressure differential into kinetic energy for controlling the upper surface separation.

This report presents the results of this investigation conducted in the California Institute of Technology Merrill Wind Tunnel. A brief description of the tunnel is given in Appendix I.

II-MODEL, APPARATUS, AND TESTS

The investigation described herein was conducted on a 10% thick double-wedge airfoil with a 15% leading-edge slat. Two movements were used to position the slat, namely, rotation about the 15% chord point and radial translation which allowed variations in the slot gap (cf. Fig. 2). Rotation of the slat was similar to a hinged nose and limited the scope of the testing to slat chord positions on radii of the 15% chord point. Radial movement permitted variations of the slat slot-gap exit, g in figure 2, although the slot contour was not variable beyond the allowances of these two movements. No trailing edge high lift device was used in this investigation.

A sketch of the model is given as figure 1 and a section with details of the slat and pressure taps together with coordinates of the slat slot is given in figure 2. The pressure taps, #80 drill holes in the model surface, were connected at one end of the model, via plastic tubing, to a multiple manometer board. The model was machined from brass bar stock and held together with locking devices and screws. The two circular end plates fastened on the ends of the 8" chord 24" span model were cut from 0.125" 24ST aluminum. In these end plates, circular slat-end support discs were mounted flush with the inner surface through circular cutouts. Slots in these support discs permitted the radial movement. Additional slat support was given by four pins rigidly attached to the slat and locked by a device located in the main section which also permitted the slat rotation and translation movements (Fig. 2a). The model was mounted conventionally on a three point balance suspension system with the bayonet trunnions on the outside of the endplates and the rear support in the center of a cross bar between arms fastened to the endplates.

The test program was conducted in three phases as follows:

a) Force data were measured directly by the balance system and were corrected by support system aerodynamic tares taken with the model removed. Of the three two-dimensional force components, the largest corrections were applied to the drag force while the lift and pitching moment corrections were nearly insignificant. While the conditions with the model removed did not exactly duplicate the flow on the inner surfaces of the endplates or the downwash on the rear support with the model present, it was felt that this approximation permitted reasonably good quantitative evaluation of the force coefficients.

Variations of slat angular rotation and radial translation were made to determine the optimum lift conditions and to determine the relative merits of these two movements. Optimum positions were attained only for the nose angles of 25, 30, and 35 degrees.

b) Pressure distributions were recorded with the slat in the various positions primarily to check the effectiveness of the slot and secondarily to determine the mode of stalling. Readings from the 40 pressure points on the model were reduced to the dimensionless pressure coefficient C_p from manometer board photograph negatives. To determine the slot effectiveness, the slot of the slat was sealed on the bottom side with scotch tape to prevent air flow through the slot and the runs repeated. Since the pressure taps were in fixed positions on the surfaces, the various peak and transition pressures occurring especially about the nose and slot of the model were not exactly determined. The reference point for the pressure coefficients was taken as the static pressure ring at the throat entrance and therefore the pressure coefficients are only for relative information rather than for absolute magnitudes.

c) Tuft studies on the model were conducted to indicate the mode of stall separations on the upper surfaces and also the effectiveness of the slot in preventing separation. Four rows of tufts were used; one on the slat, another on the main section ahead of the wedge peak and the other two behind the peak. Comparison of sealed and unsealed slot conditions and of successively increasing angles of attack showed quite well the slat effectiveness and stall development.

III-DATA PRESENTATION

Aerodynamic force data obtained from the balance system were corrected only for the dynamic forces acting on the support system and not for the wind tunnel wall influences and buoyancy since the tests were primarily comparative. Figure 3 summarizes the variations of Cl_{max} with slat angular rotation and translation. It is to be noted that the sensitivity of the maximum lift coefficient was more a function of the added camber due to the angular movement than of slot width variations from radial translation with the exception of the 30° and 35° nose angles. These curves were taken from the aerodynamic polars that follow in figures 4 through 9. Each figure is for a given nose angle with the slat radial translation as the variable. In this series of curves, the gap of the slot exit was increased from the minimum to that obtainable with slat position 7. The data are shown as measured at the 50% chord point, with corrections for the support system as previously mentioned. In figure 10 the data for slat position 7 and all nose angles are shown as resolved about the quarter-chord point, i.e., the pitching moment has been transferred from the 50% chord point to the 25% chord point. Figures 11 and 13 give the effects of moving the slat beyond the optimum condition for the nose angles of 25°, 30°, and 35°.

The next series of figures, numbered 14 through 23, are plots of pressure coefficient profile variations with the slot sealed and unsealed at the same angles of attack and furnish some comparisons of approximately the one-half and full maximum lift conditions. The dashed lines indicate areas of transition where a proper estimation of the coefficient variations was not possible. These areas were across the slot openings, and on both the top and bottom surfaces of the slat nose where quite large changes in the pressure coefficients were experienced.

Variations of the pressure coefficient profiles with angle of attack for configuration 7-35 which was very near to the optimum high lift arrangement are presented as figures 24 through 30. The range of attack angles was from zero to twenty-eight degrees and passed beyond the maximum lift point. These curves show not only the velocity characteristics over the airfoil and the separation areas but also characterize the moment variations.

The last of the pressure coefficient curves, figures 31 to 34, indicate the conditions beyond the optimum slot openings for the given nose angles. They are indicative of the points of failure for the slot in controlling the flow over the upper surface of the airfoil.

IV-RESULTS AND DISCUSSION

The curves of figure 3 summarize results obtained for $C_{l_{max}}$ from the force measurements and indicate that the nose deflection or slat rotation was the major factor for increasing the maximum lift coefficient with the lower nose angles. However, at the nose angles of 30° and 35°, the slot gap variation played the more important role for increasing $C_{l_{max}}$. Optimum conditions of slot gap were attained for the nose angles of 25°, 30°, and 35° where increasing nose angles produced approximately a linear increment in the optimum lift coefficient. For the lower nose angles, the optimum conditions were not reached, but the tests indicated that sizeable gains might be achieved by further increases in the slot gap.

The initial opening of the slot for the nose angles of 10° and 20° produced increments of lift at all attack angles (Figs. 5 and 6). The zero nose angle, however, caused lift decrements until beyond the stall angle of the basic section (Fig. 4). At the higher nose deflections, i.e., 25°, 30°, and 35°, the lift decreased slightly with increasing slot gap to a transition point below $C_{l_{max}}$ where the increasing gap increased lift. These changes in the lift coefficient with gap variations were small in all cases with the exception of the 30° and 35° nose angles which were more critical to the gap adjustment.

The pressure profile curves provided an explanation for this phenomenon as seen in figure 14 for the zero nose angle and various slot gaps. As the slat was moved radially to increase the slot gap, the changes in the pressure coefficient profiles were noticed: first, the pressure coefficient increased on the slat upper surface and, second, behind the slot and ahead of the wedge peak, the velocity decreased. Since the measured lift coefficients at this angle of attack decreased only a small amount, the two effects nearly cancelled each other. A decreased velocity behind the slot rather than the desired increase in velocity was attributed to the separation occurring at the nose. Reference 3 indicates that the separated region for a 4.5% modified double wedge at an angle of attack of 8^o extended over the entire upper surface of the airfoil. If this may be applied to the case at hand, then kinetic energy additions from the slot air to the upper surface boundary layer must tend to cause reattachment over the entire upper surface. Also, the pressure differential of the wedge section is relatively small over the sharp nose surfaces, so less potential energy is available for conversion to kinetic energy. In figure 35, the sketches of the separated regions for 7-0 and 7_s-0 show that the slot partially caused reattachment of the nose flow separation while the entire upper surface air flow separated with the slot sealed. At higher nose deflections the pressure differential between the upper and lower slot openings increased and therefore the kinetic energy of the slot air was increased. Also, since the pressure gradient over the cambered upper surface was more favorable to the flow, the energy required to control separation was less because the nose separation was confined to the slat surface. For these reasons, it was found that the slot was more effective in controlling separation with greater nose angles.

Starting with the 25° nose angle, the lift curve developed a break in the linear portion of the curve. The slope of the lift curve beyond this break decreased as a function of the nose angle. While the break was more pronounced for the narrower slot gaps, it was quite consistent for all configurations. Each of three causes seemed to be partially responsible for this lift curve behavior. First, the break occurred when separation started from the trailing edge of the airfoil. This happened approximately at an angle of attack of 12° for all three nose angles and was substantiated by the tuft sketches and also the pressure curves for the configuration 7-35 (cf. figures 26 and 27). Second, in this region of attack angles the airfoil nose stagnation point moved from the upper surface to the lower surface of the slat. This caused an adverse pressure gradient on the upper surface of the slat and thus initiated nose flow separation. These changes about the nose were a function of the nose angle and accounted in part for the decrease in slope of the lift curve after the break with increasing nose angle, i.e., their effects on the lift curve were more pronounced with the nose deflected to a greater angle. Third, because of this stagnation point movement, the pressure forces acting upward on the model slat became very much larger. This caused the slat to bow in the middle by bending the support pins and created a slippage problem with the locking system until in certain instances the slot gap was nearly double in the middle compared to the original setting. Time did not allow this situation to be remedied. The effect of this item was noticed in the three figures of tuft pattern sketches as curvature in the separated regions denoted by the shaded areas. The end discs held the slat to the correct gap and therefore the portions of the patterns near the end plates were more nearly correct. Unfortunately, there was no method of evaluating the lift losses incurred by each of these causes, but much improvement should be expected by holding the slat to the preset position. Figure 9 configuration 5_s-35 shows that the failure of the plain nose flap occurred in the same angle of attack region as the break in the lift curve. Therefore it was presumed that the causes of the stall of the airfoil with a plain nose flap were evidently responsible for the break in the lift curve for the slatted airfoil, but were partly eliminated or counteracted by the slot.

One of the most noticeable advantages of the slat over the nose flap was the manner in which the model stalled. At the stall for the nose flap, the drag would start to increase quite rapidly and the pitching moment would start moving in the negative direction. Then without further warning, the entire upper surface flow commenced to separate intermittently and the result was severe buffeting. In most cases with the slot sealed, the testing limitation beyond $C_{l_{max}}$ was this buffeting condition. On the other hand, the slot was very effective in producing a smooth stall completely without oscillating flow separation and the tests were carried easily beyond the stall condition. Only with the slat moved beyond the optimum slot gap was the buffeting encountered as a limiting factor, and then it was not nearly as severe as with the slot sealed, probably because it occurred at lower lift coefficients. Tufts on the model during the slat runs did not show the tendency to fluctuate rapidly between the separated and unseparated areas, but rather the separations that occurred were distinct and their progression was strong. By comparison, the sealed nose flap tuft patterns of the separated areas had the appearance of not being as well established and near the points where the buffeting started they were rather unstable.

Changes in the force polars for the configurations with the slat in the seventh position are shown in figure 10. The shift in the zero lift angle in the positive direction, the decrease of drag at the higher lift coefficients, and the movement of the moment curves in the negative pitching direction are all typically related to the increase in camber of the airfoil by the increased nose deflection. With the exception of the 30° and 35° nose angles, the increases in angle of attack required for zero lift were approximately a linear function of the nose angle. As is usually typical of moments transferred between chord points by lift and drag component corrections, there was considerable point scatter and the curves were not too accurate. However, the drag curves were quite good in the matter of point scatter and while the tare corrections to the drag coefficients were of the same magnitude as the coefficients themselves, the corrected drag coefficients were probably within the accuracy of the balance system. The drag decreased considerably with the increasing nose angles except at low attack angles and resulted in higher lift with lower drag at the same angle of attack with increasing nose angles, except in the case of two nose angles 30° and 35° which ultimately produced more lift with less drag. These curves show that the slat extended the lift curves to higher values in the same manner as for a conventional airfoil until the nose angle reached 30°. Then the break in the lift curve caused the extension to occur with a decreased slope and presumably gave a slightly lower value of $C_{l_{max}}$ than would have occurred if the cause of the break had been completely corrected by the slat.

Additional information for the optimum condition of the slat is given by figure 38 as variations of the pressure coefficient with angle of attack for slot taps on the slat and main section chord lines. These curves are indicative of the pressure differential or potential energy of the slot. According to the graph, the slot flow steadily increased to an optimum value at an angle of attack of 18°. The pressure on the slot exit increased for greater attack angles causing a reduction in the slot pressure differential and presumably in the flow. Coincidently at 18°, the stagnation point on the airfoil moved to the bottom surface of the slat and the break in the lift curve caused a reduced rate of lift increase with angle of attack (cf. Figs. 9, 28, 29, and 38).

An interesting sidelight is offered by reference 4 on the investigation of a 9% 6-series airfoil with a 15% nose slat.

Within the limits of the investigation, it was found that the optimum slat position was an angle of 24.3° and a gap of 0.6%c. This compared in the following manner with the slatted double wedge:

	$c_{l_{max}}$	α_u	$c_{l_{max}}$	$\Delta\alpha_u$	a	g
Double Wedge (7-30)	1.28	20°	0.57	10°	30.0°	0.8
NACA 65A109	1.86	21°	0.69	10°	24.3°	0.6

The NACA tests were run at a Reynolds number of 6.0×10^6 and the lift coefficients are uncorrected for blocking. While the above figures are for the optimum slot gap, they are not necessarily for the optimum slat rotation.

V-CONCLUSIONS

The results of a two-dimensional wind tunnel investigation at a Reynolds number of 0.78×10^6 of a 10% double wedge airfoil equipped with a 15% chord leading edge slat produced the following conclusions:

a) The lift curve is extended to a higher maximum lift coefficient at a higher angle of attack. This extension occurred at the same slope as for the plain nose flap except for the nose angles of 25°, 30°, and 35°, where it was extended at a lower slope dependent on the nose angle.

b) The drag and pitching moment for the various nose angles behaved in the manner typical of increases in airfoil camber; the slot apparently had little effect on either of these forces. Reductions in drag were noted at high angles of attack for the cases of open slot with the larger nose angles.

c) The slot definitely aided in controlling the boundary layer behind the slat. The stall for the optimum slot conditions was a result of the trailing edge separation moving forward over the entire upper surface in the normal manner.

d) The slot air-flow kinetic energy additions to the upper surface boundary layer almost completely eliminated the buffeting encountered in the case of the airfoil with the plain nose flap.

e) Stall conditions with the slat extended were made more gradual than for either the basic section or the plain nose flap.

VI-REFERENCES

1) Rose, Leonard M., and Altman, John M.: Low-Speed Experimental Investigation of a Thin, Faired, Double-Wedge Airfoil Section with Nose and Trailing-Edge Flaps. NACA TN 1934, 1949.

2) Rose, Leonard M., and Altman, John M.: Low-Speed Investigation of a Thin, Faired, Double-Wedge Airfoil Section with Nose Flaps of Various Chords. NACA TN 2018, 1950.

3) Rose, Leonard M., and Altman, John M.: Low-Speed Investigation of the Stalling of a Thin, Faired, Double-Wedge Airfoil with Nose Flap. NACA TN 2172, 1950.

4) Gottlieb, Stanley M.: Two-Dimensional Wind-Tunnel Investigation of Two NACA 6-Series Airfoils with Leading-Edge Slats. NACA RM No. L8K22.

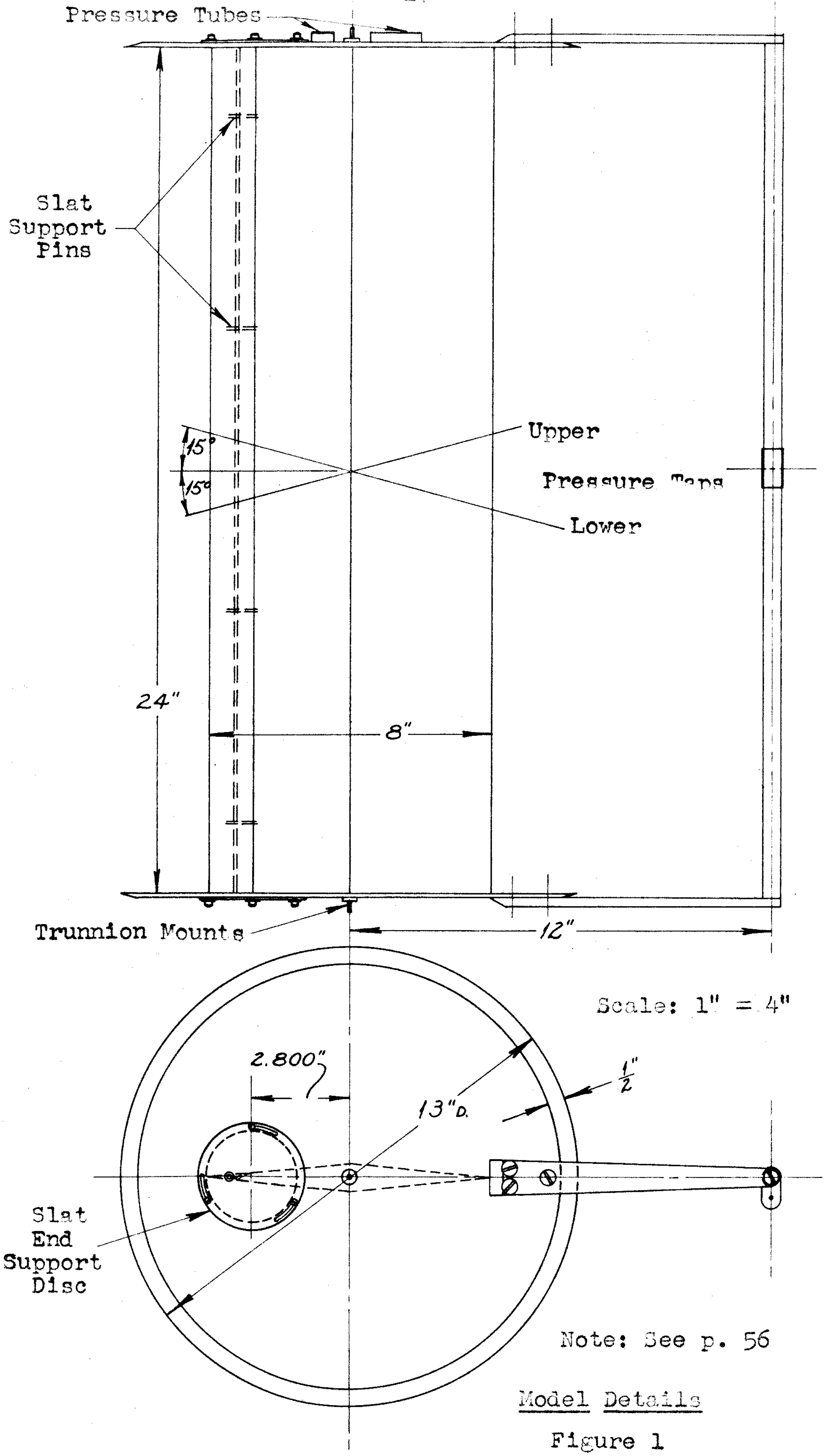

Scale: 1" = 4"

Note: See p. 56

Model Details

Figure 1

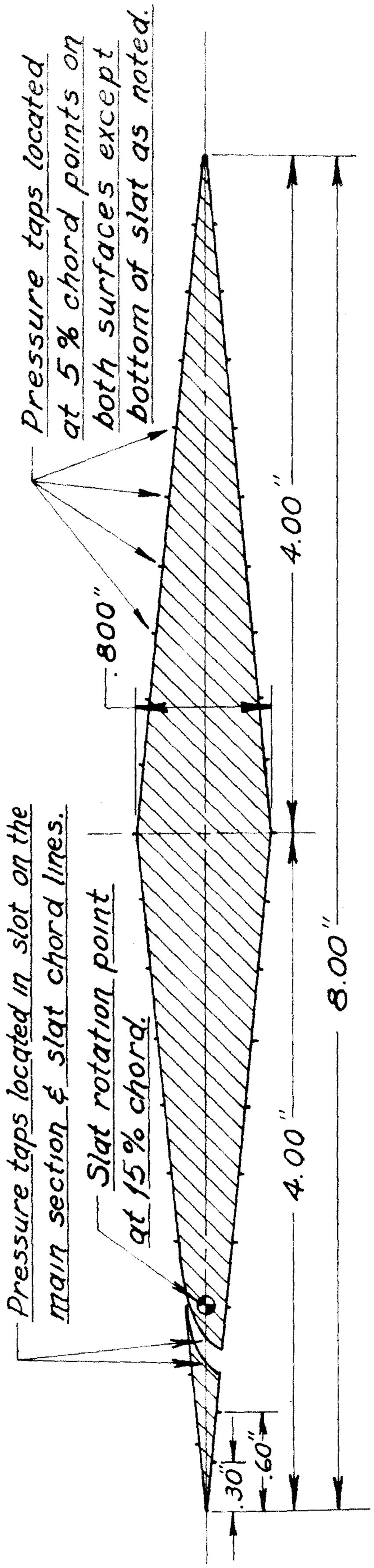

MODEL SECTION
Full Scale

Slot Coordinates in Percent Chord		
y- ord.	front x- ord.	rear x- ord.
1.75	---	17.65
1.50	15.00	16.35
1.25	13.75	15.35
1.00	13.70	14.53
0.75	11.95	13.90
0.50	11.40	13.38
0.25	11.00	13.00
0.00	10.67	12.69
-0.25	10.38	12.42
-0.50	10.20	12.24
-0.75	10.05	12.11
-1.00	10.00	12.03

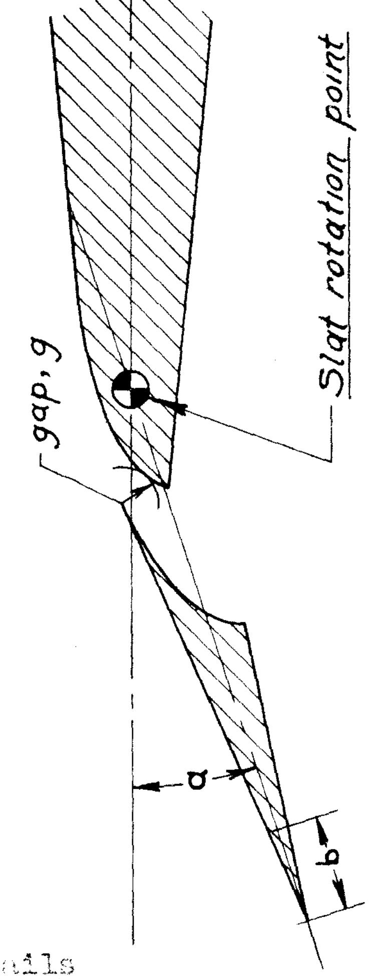

MODEL CONFIGURATION NOTATION b-a

b = Slat translation (Appendix II)

a = Slat rotation angle in degrees

Note-Subscript s on b indicates slot was sealed, ie., b_s-a

Airfoil Section Details

Figure 2

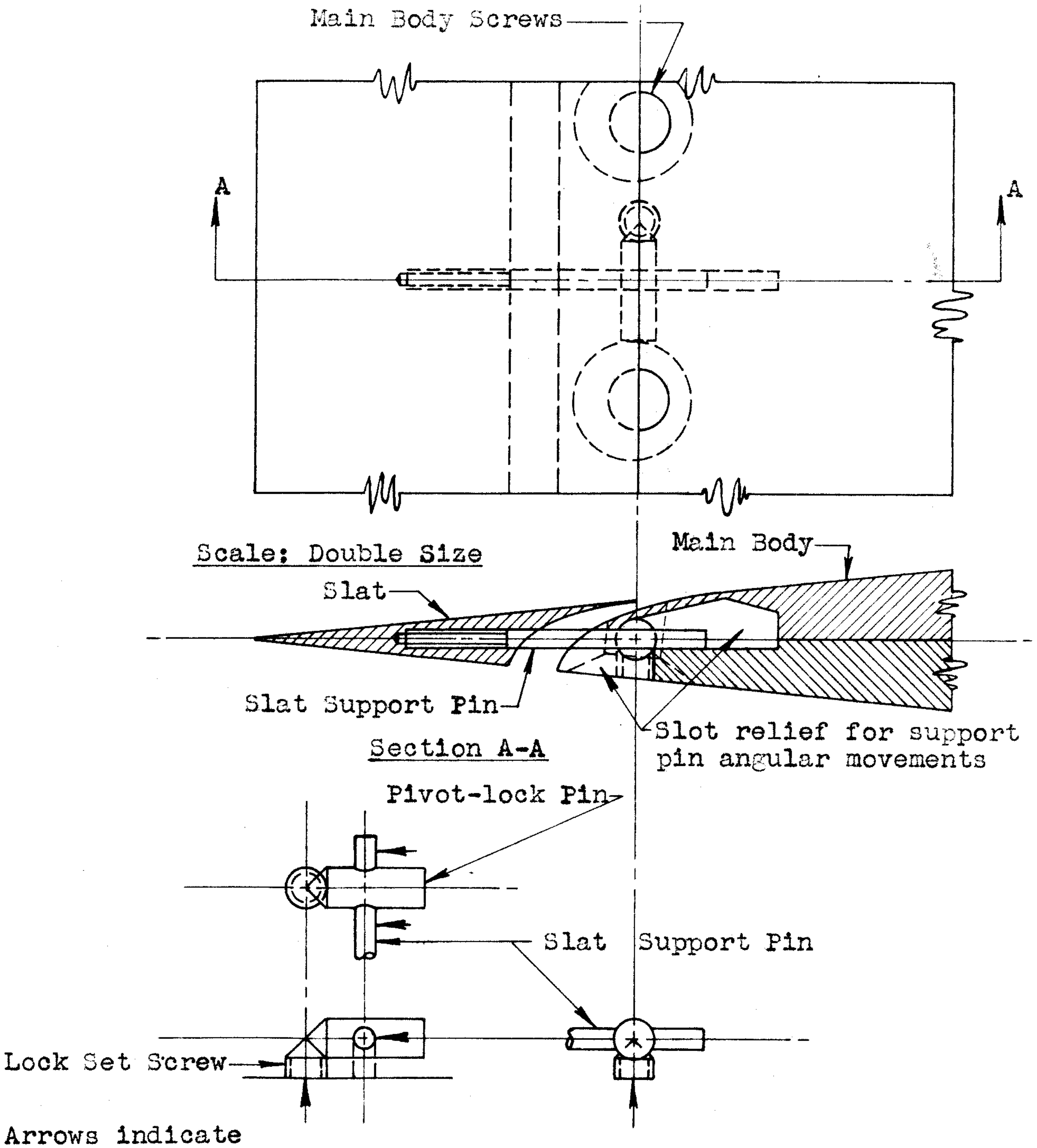

Scale: Double Size

Arrows indicate locking forces

Detail of Locking Pins

Working principle: The set screw inclined face locks the support pin against the slot face.

Details of the Slat Support
Figure 2a

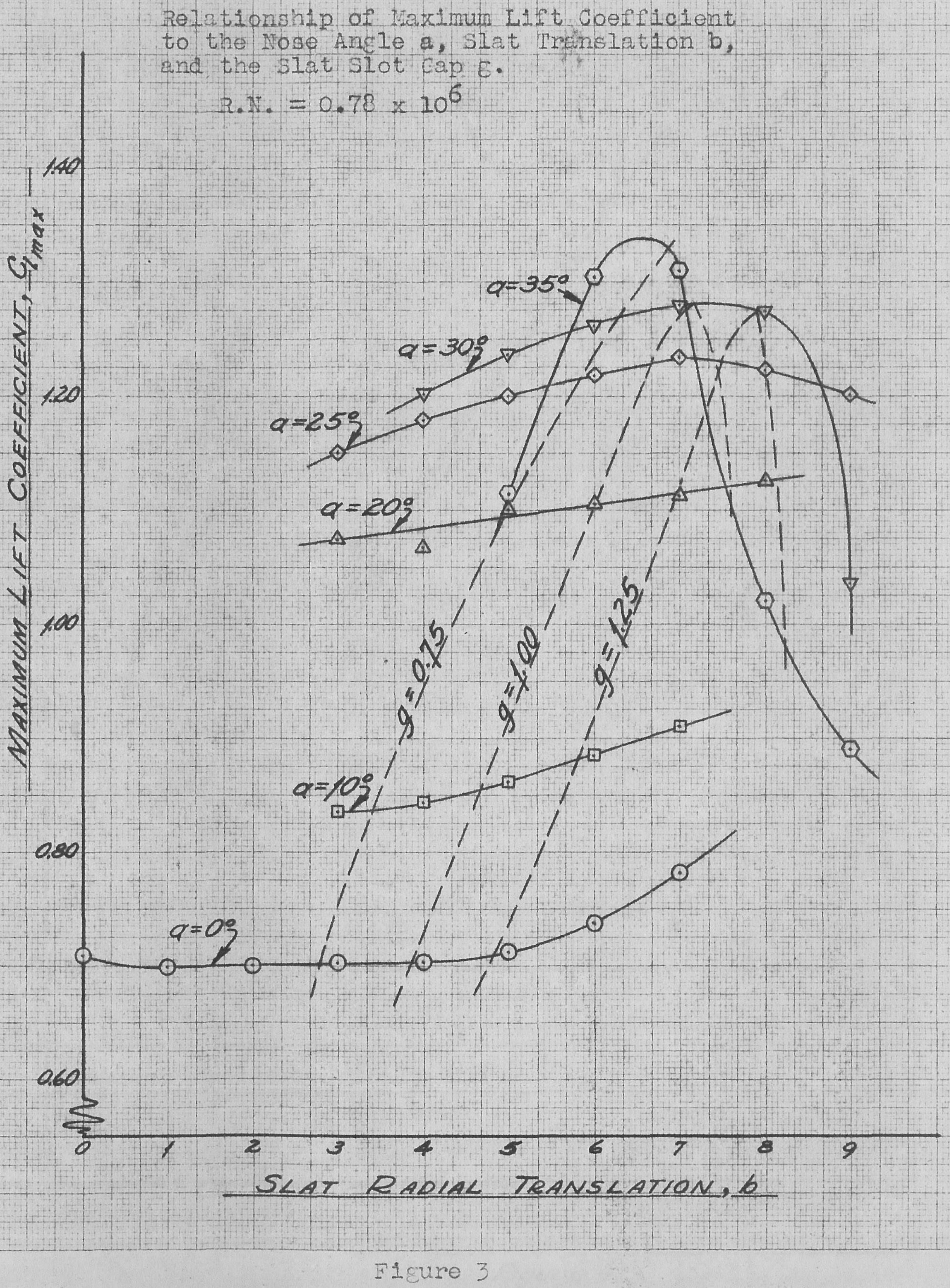

Relationship of Maximum Lift Coefficient to the Nose Angle a, Slat Translation b, and the Slat Slot Cap g.

R.N. = 0.78×10^6

Figure 3

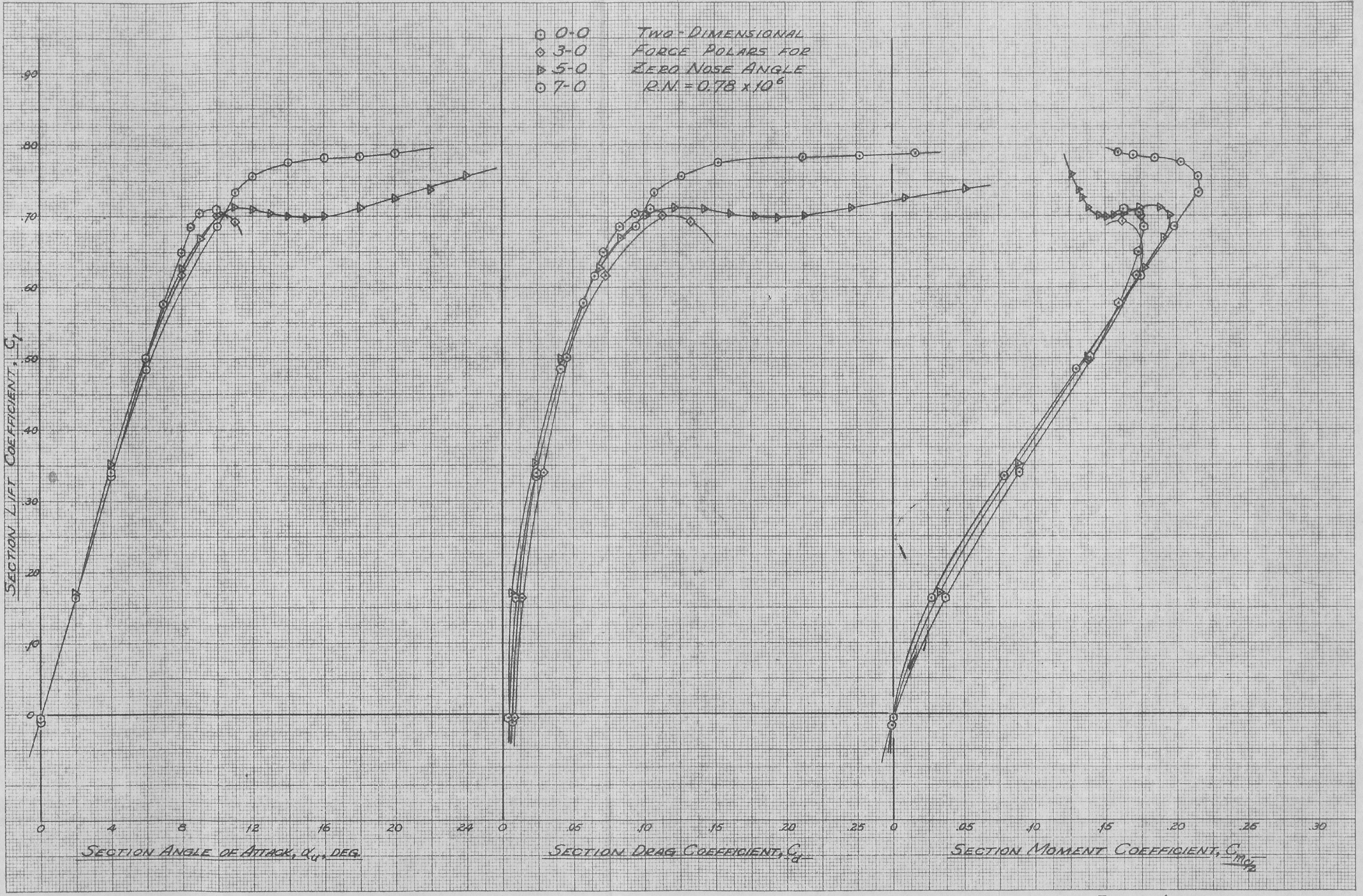
⊙ 0-0
◇ 3-0
▷ 5-0
⊙ 7-0
Two-Dimensional
Force Polars for
Zero Nose Angle
R.N. = 0.78 x 10^6
Section Lift Coefficient, C_l
.90
.80
.70
.60
.50
.40
.30
.20
.10
0
0
4
8
12
16
20
24
Section Angle of Attack, α_u, deg.
0
.05
.10
.15
.20
.25
Section Drag Coefficient, C_d
0
.05
.10
.15
.20
.25
.30
Section Moment Coefficient, C_m c/2

Figure 4

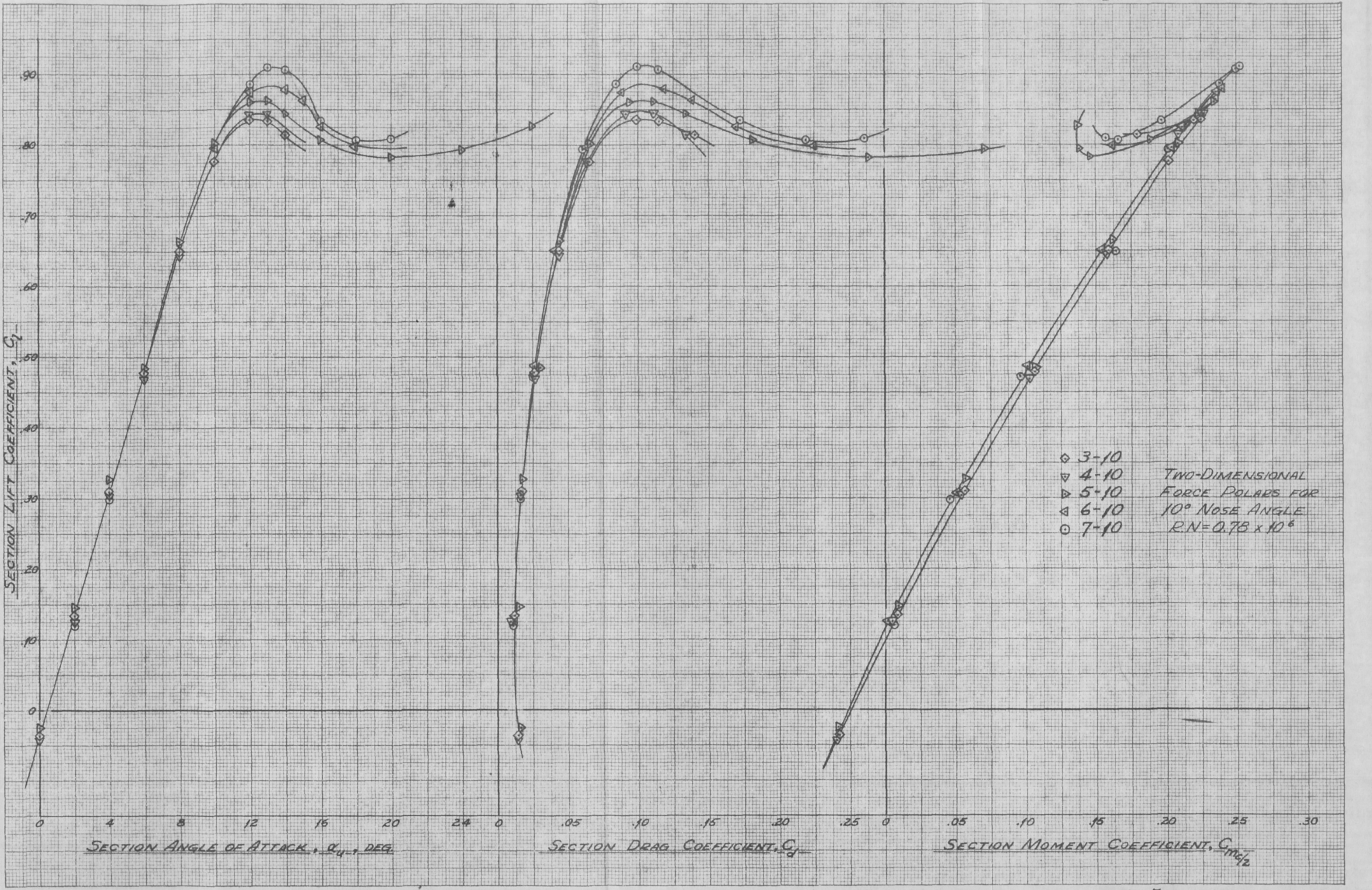
SECTION LIFT COEFFICIENT, C_l
.90
.80
.70
.60
.50
.40
.30
.20
.10
0
0
4
8
12
16
20
24
SECTION ANGLE OF ATTACK, α_o, DEG.
0
.05
.10
.15
.20
.25
SECTION DRAG COEFFICIENT, C_d
0
.05
.10
.15
.20
.25
.30
SECTION MOMENT COEFFICIENT, $C_{m_{c/2}}$
◇ 3-10
▽ 4-10
▷ 5-10
◁ 6-10
⊙ 7-10
TWO-DIMENSIONAL
FORCE POLARS FOR
10° NOSE ANGLE
R.N = 0.78 × 10⁶

Figure 5

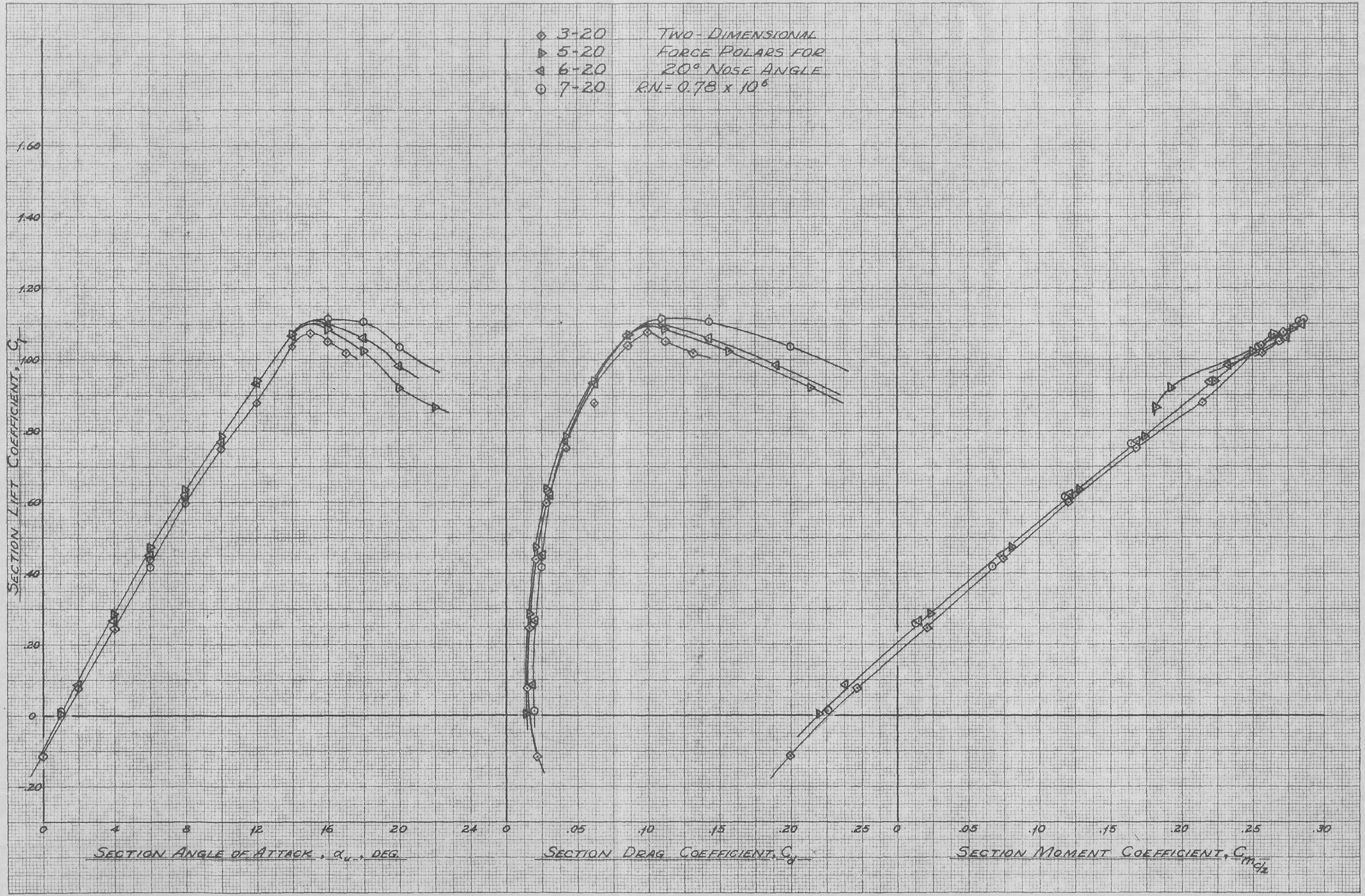
◇ 3-20
▷ 5-20
◁ 6-20
○ 7-20
TWO-DIMENSIONAL
FORCE POLARS FOR
20° NOSE ANGLE
R.N. = 0.78 x 10⁶
1.60
1.40
1.20
1.00
.80
.60
.40
.20
0
-.20
SECTION LIFT COEFFICIENT, C_l
0
4
8
12
16
20
24
SECTION ANGLE OF ATTACK, α_u, DEG.
0
.05
.10
.15
.20
.25
SECTION DRAG COEFFICIENT, C_d
0
.05
.10
.15
.20
.25
.30
SECTION MOMENT COEFFICIENT, $C_{m_{c/2}}$

Figure 6

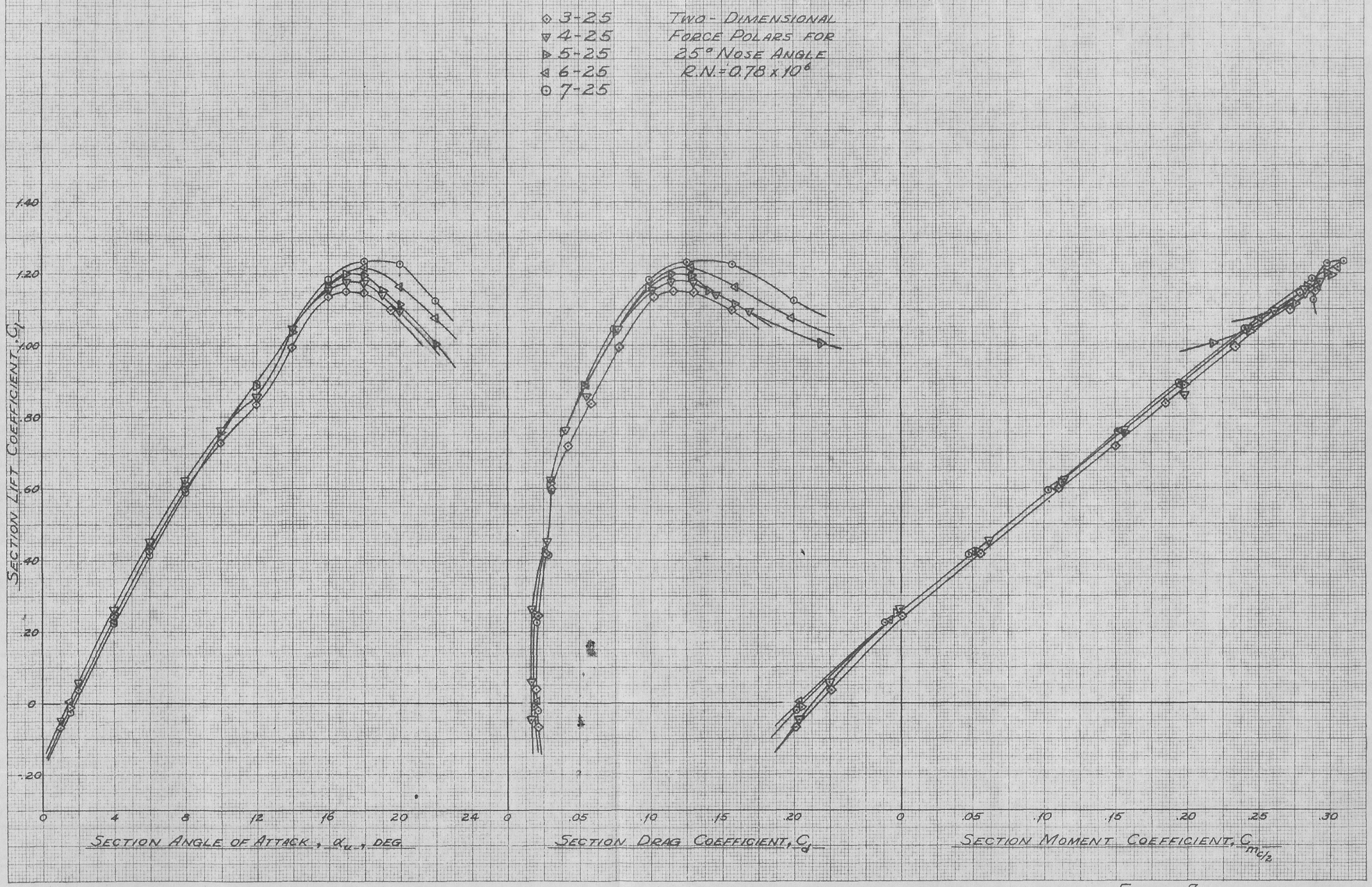
◇ 3-25
▽ 4-25
▷ 5-25
◁ 6-25
⊙ 7-25
Two-Dimensional
Force Polars for
25° Nose Angle
R.N.=0.78 x 10^6
Section Lift Coefficient, C_l
1.40
1.20
1.00
.80
.60
.40
.20
0
-.20
0
4
8
12
16
20
24
Section Angle of Attack, α_o, deg
0
.05
.10
.15
.20
Section Drag Coefficient, C_d
0
.05
.10
.15
.20
.25
.30
Section Moment Coefficient, $C_{m_{c/2}}$

Figure 7

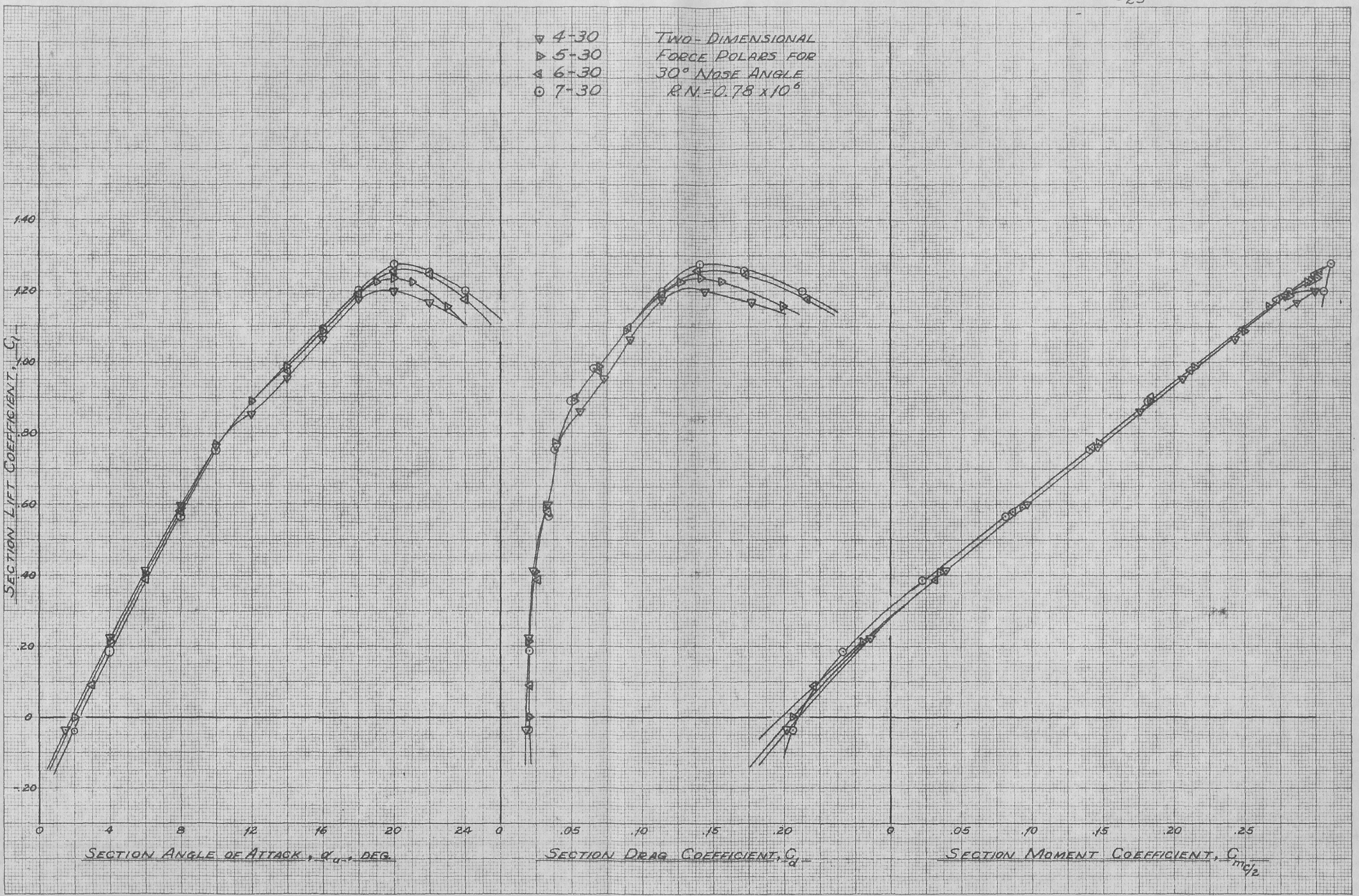
TWO-DIMENSIONAL FORCE POLARS FOR 30° NOSE ANGLE $R.N.=0.78\times10^6$

Figure 8

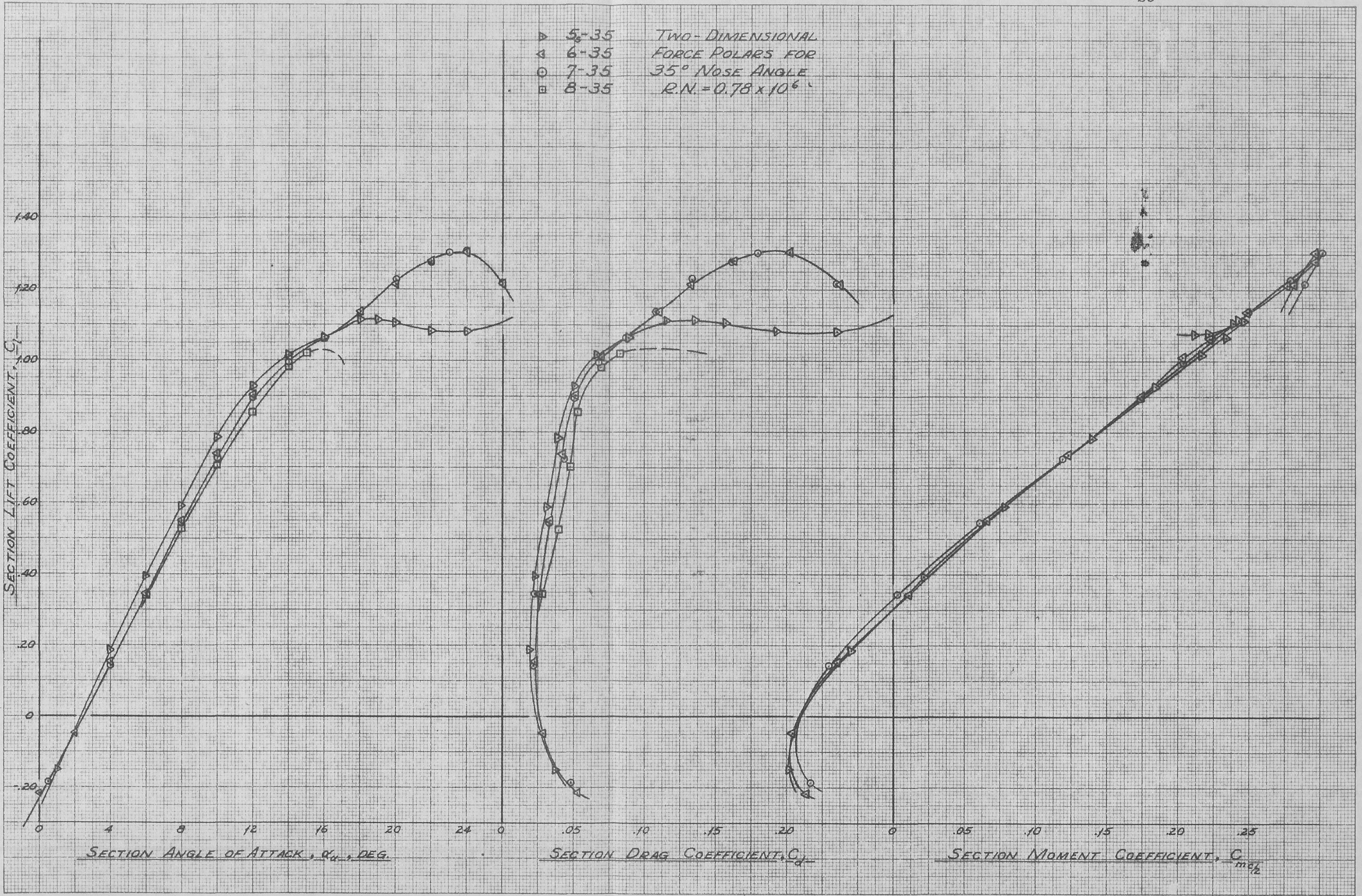
▷ 5_s-35
◁ 6-35
⊙ 7-35
⊡ 8-35
TWO-DIMENSIONAL
FORCE POLARS FOR
35° NOSE ANGLE
R.N. = 0.78 x 10^6
SECTION LIFT COEFFICIENT, C_l
1.40
1.20
1.00
.80
.60
.40
.20
0
-.20
0
4
8
12
16
20
24
0
.05
.10
.15
.20
0
.05
.10
.15
.20
.25
SECTION ANGLE OF ATTACK, α_u, DEG.
SECTION DRAG COEFFICIENT, C_d
SECTION MOMENT COEFFICIENT, $C_{m_{c/2}}$

Figure 9

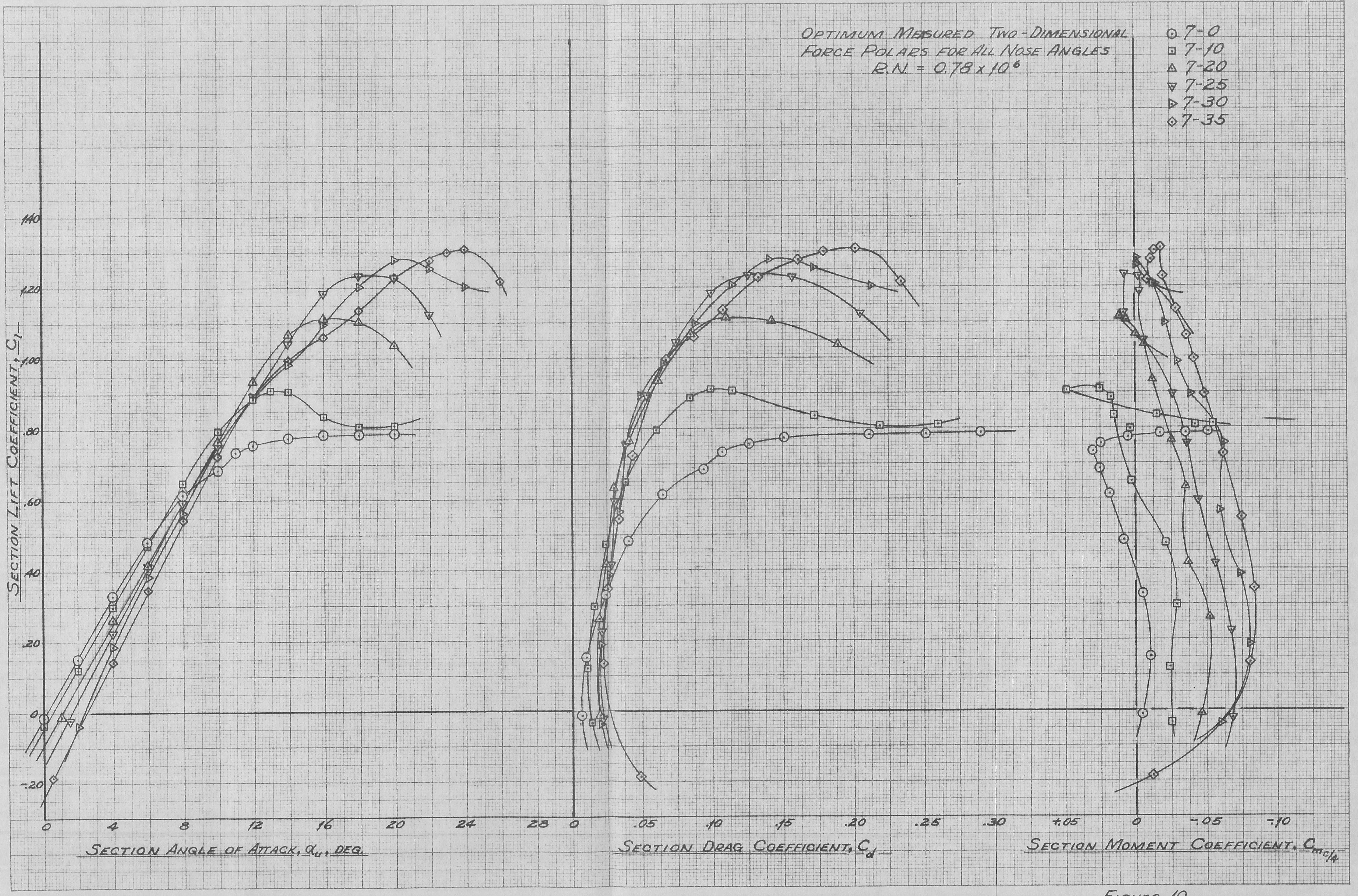

OPTIMUM MEASURED TWO-DIMENSIONAL FORCE POLARS FOR ALL NOSE ANGLES

R.N. = 0.78×10^6

Figure 10

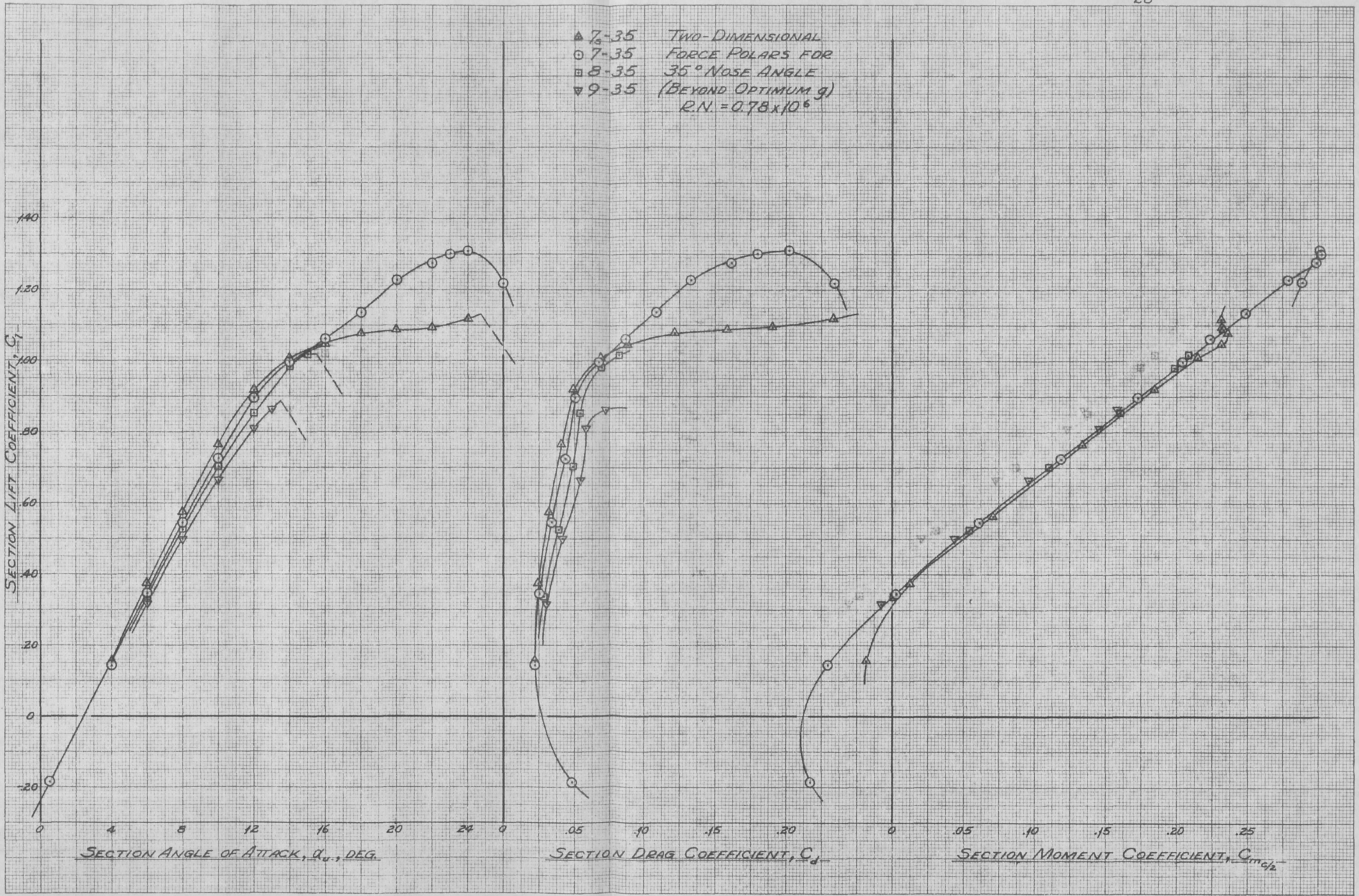

TWO-DIMENSIONAL FORCE POLARS FOR 35° NOSE ANGLE (BEYOND OPTIMUM g) R.N. = 0.78×10^6

Figure 11

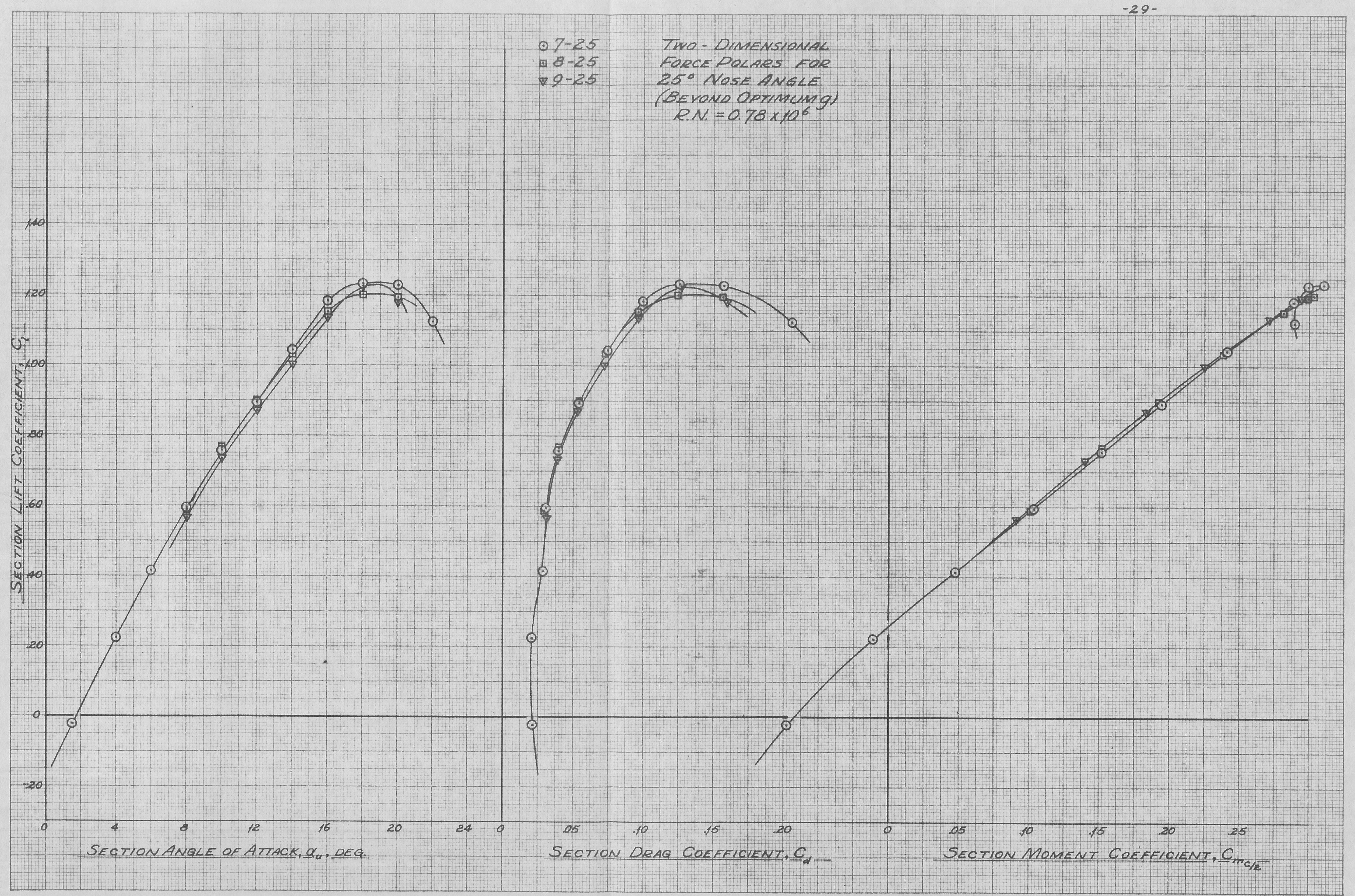
⊙ 7-25
⊡ 8-25
▽ 9-25
TWO - DIMENSIONAL
FORCE POLARS FOR
25° NOSE ANGLE
(BEYOND OPTIMUM g)
R.N. = 0.78 x 10^6
SECTION LIFT COEFFICIENT, C_l
1.40
1.20
1.00
.80
.60
.40
.20
0
-.20
0
4
8
12
16
20
24
SECTION ANGLE OF ATTACK, α_u, DEG.
0
.05
.10
.15
.20
SECTION DRAG COEFFICIENT, C_d
0
.05
.10
.15
.20
.25
SECTION MOMENT COEFFICIENT, C_m c/2

Figure 12

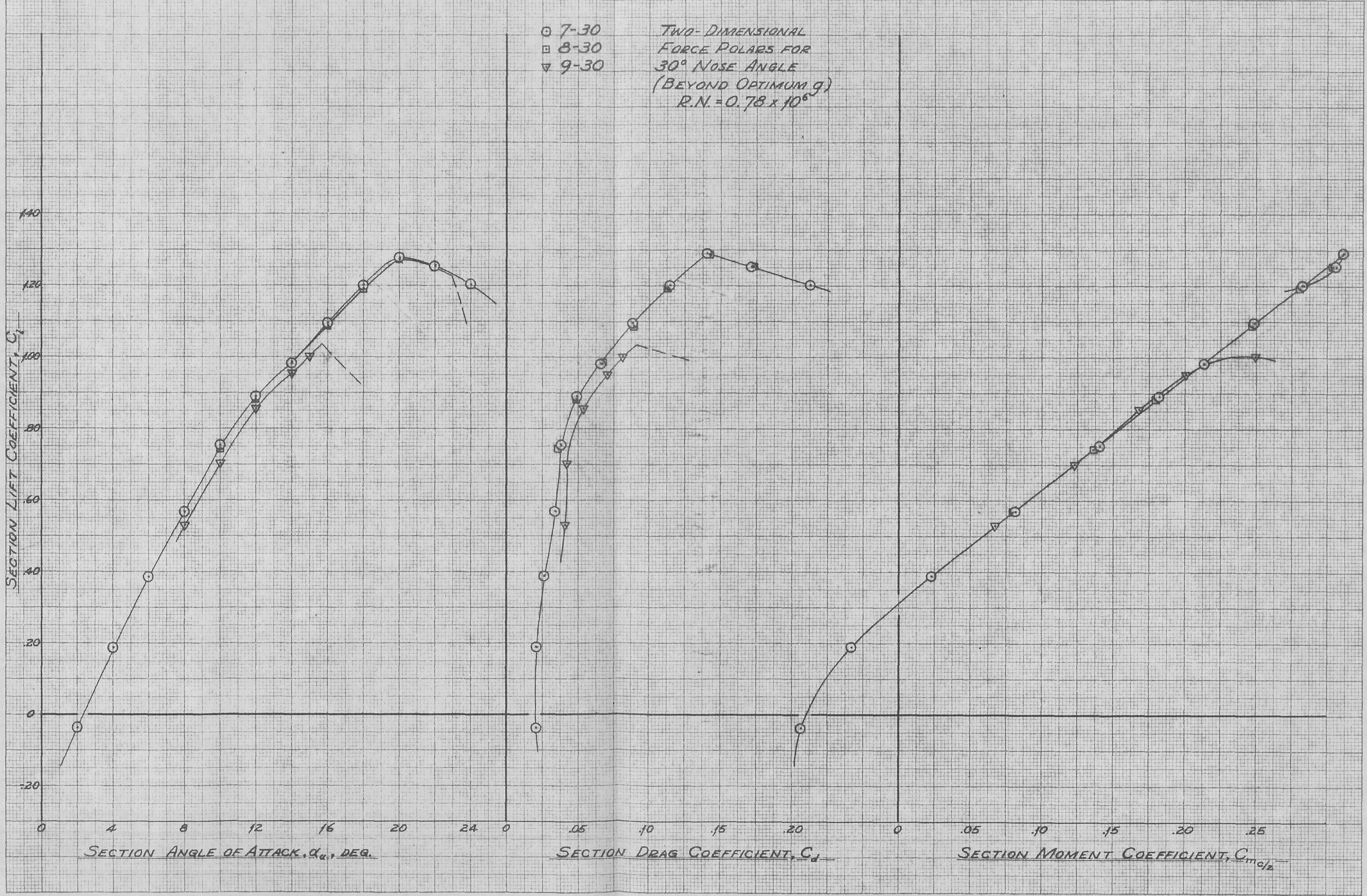
⊙ 7-30
⊡ 8-30
▽ 9-30
TWO-DIMENSIONAL FORCE POLARS FOR 30° NOSE ANGLE (BEYOND OPTIMUM g) R.N.=0.78 x 10^6
SECTION LIFT COEFFICIENT, C_l
1.40
1.20
1.00
.80
.60
.40
.20
0
-.20
0
4
8
12
16
20
24
SECTION ANGLE OF ATTACK, α_o, DEG.
0
.05
.10
.15
.20
SECTION DRAG COEFFICIENT, C_d
0
.05
.10
.15
.20
.25
SECTION MOMENT COEFFICIENT, $C_{m_{c/2}}$

Figure 13

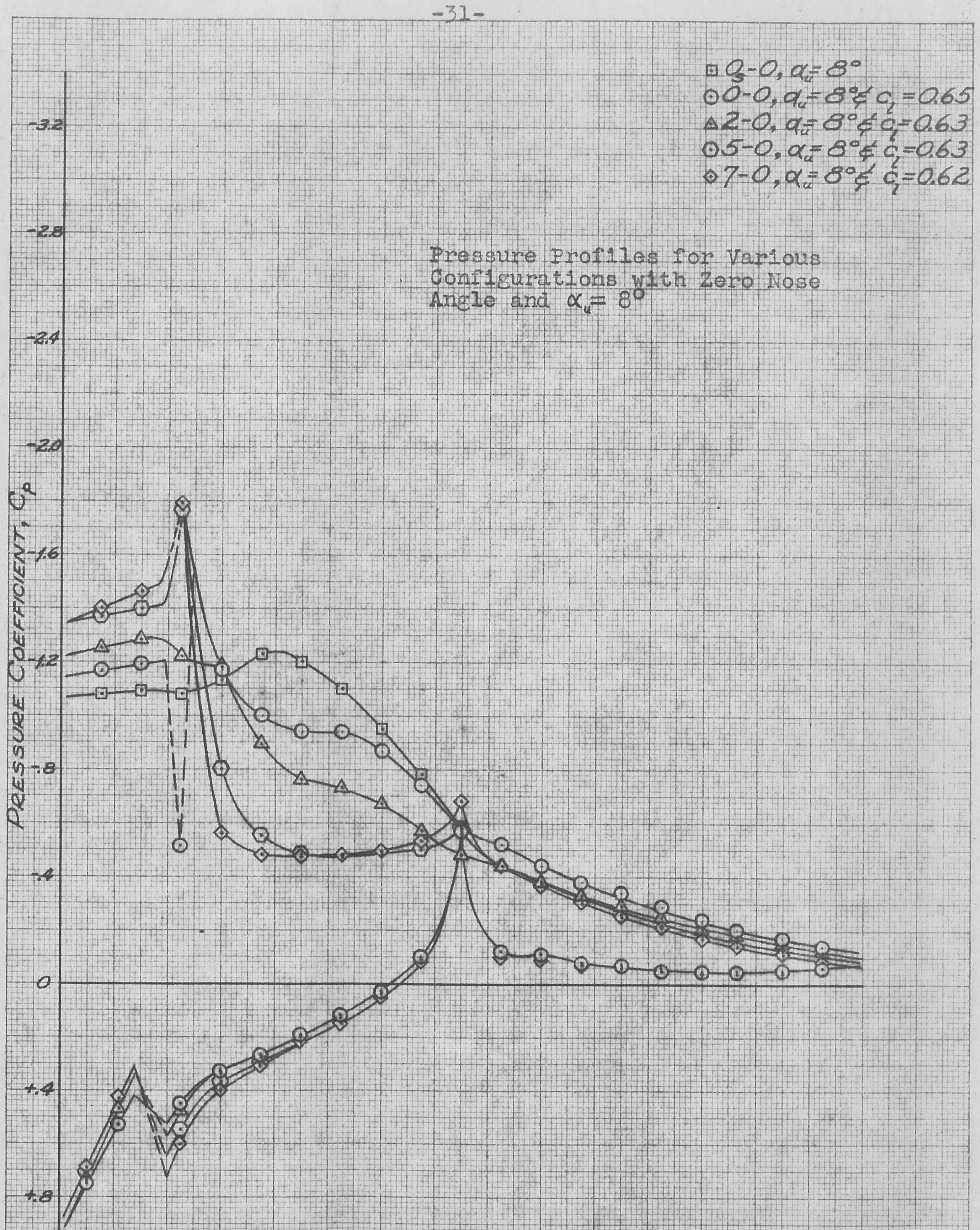

Pressure Profiles for Various Configurations with Zero Nose Angle and $\alpha_u = 8°$

Figure 14

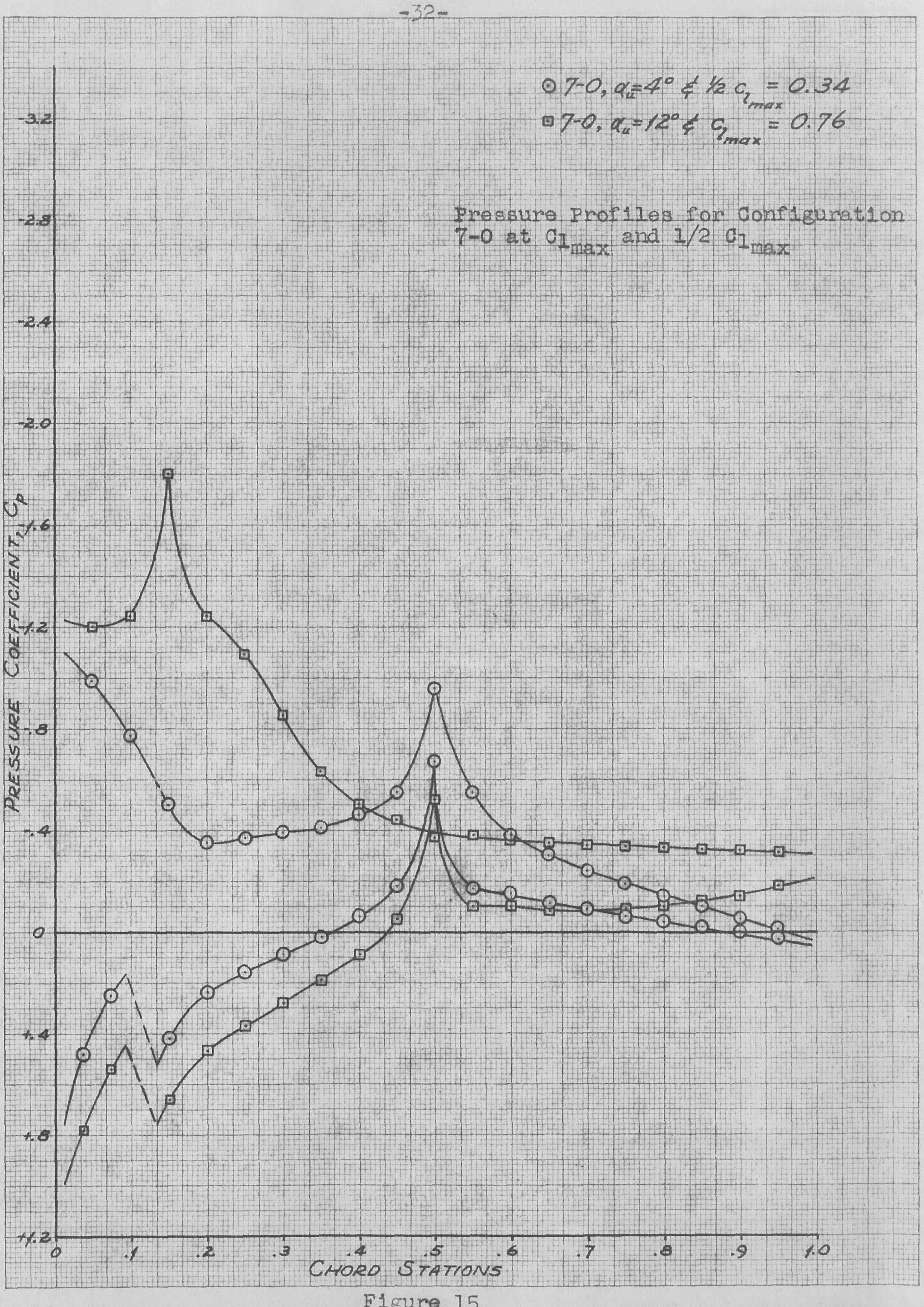

Pressure Profiles for Configuration 7-0 at $C_{l_{max}}$ and 1/2 $C_{l_{max}}$

Figure 15

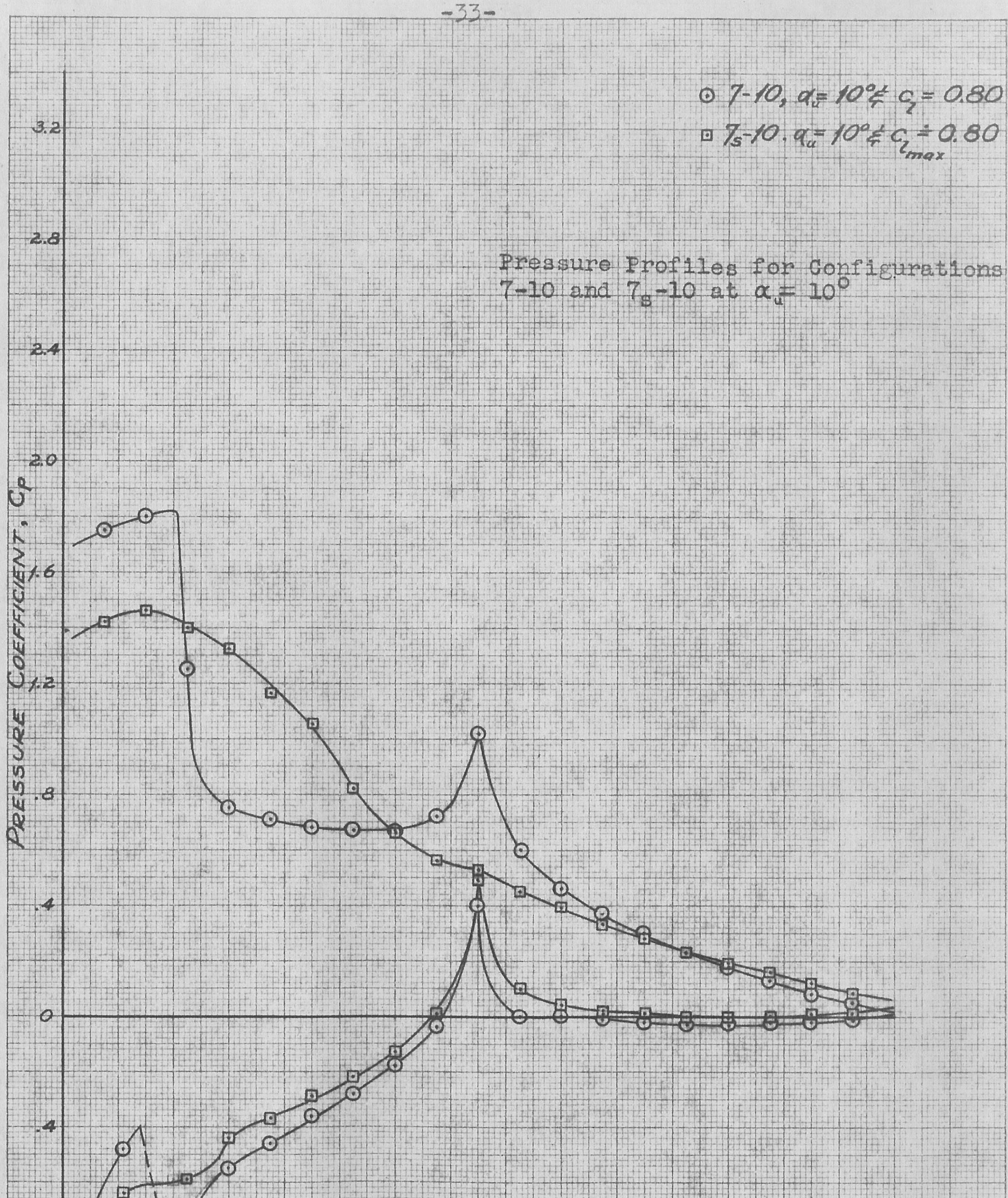
Pressure Profiles for Configurations 7-10 and 7_s-10 at $\alpha_u = 10°$

Figure 16

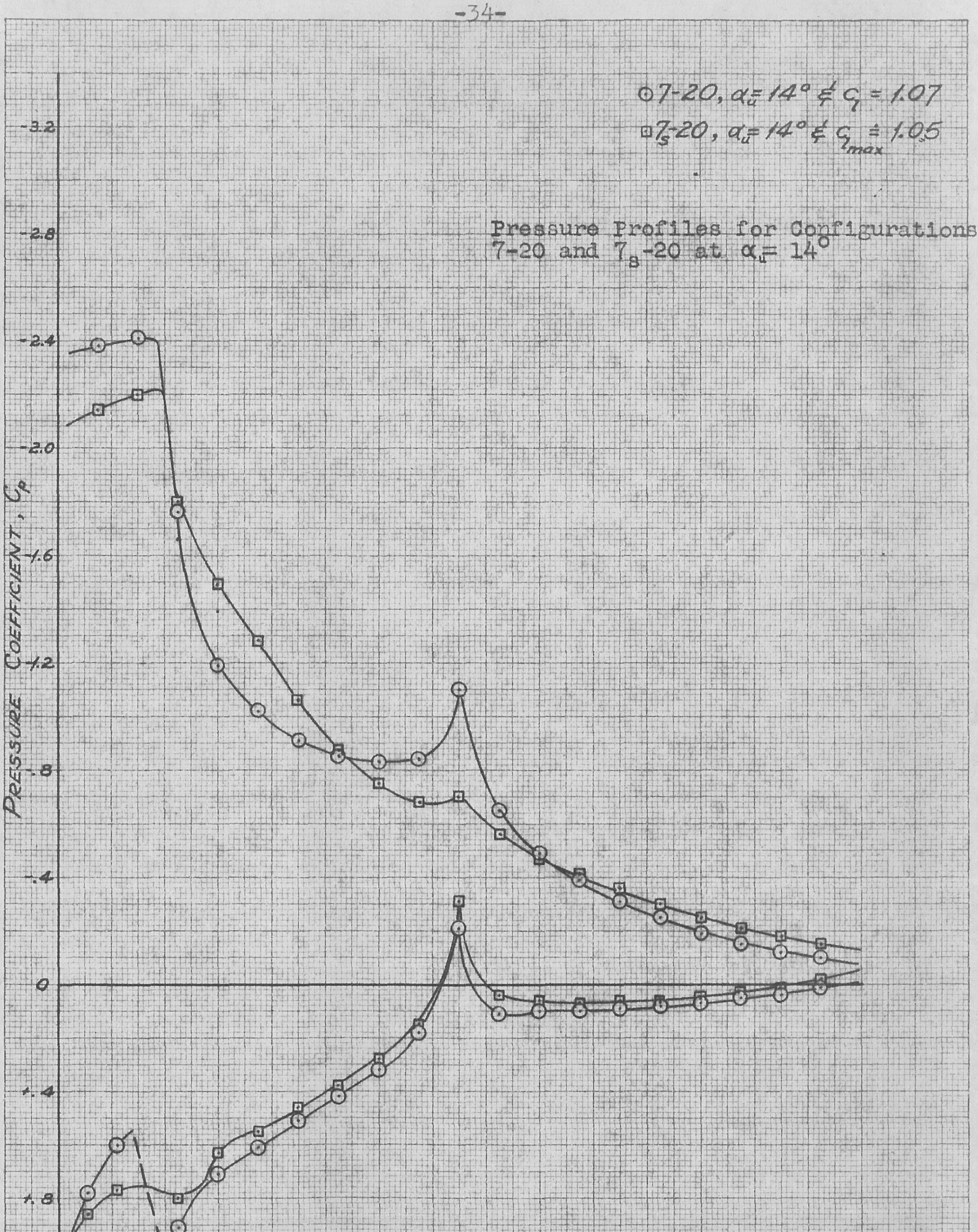

Pressure Profiles for Configurations 7-20 and 7_s-20 at $\alpha_u = 14°$

Figure 17

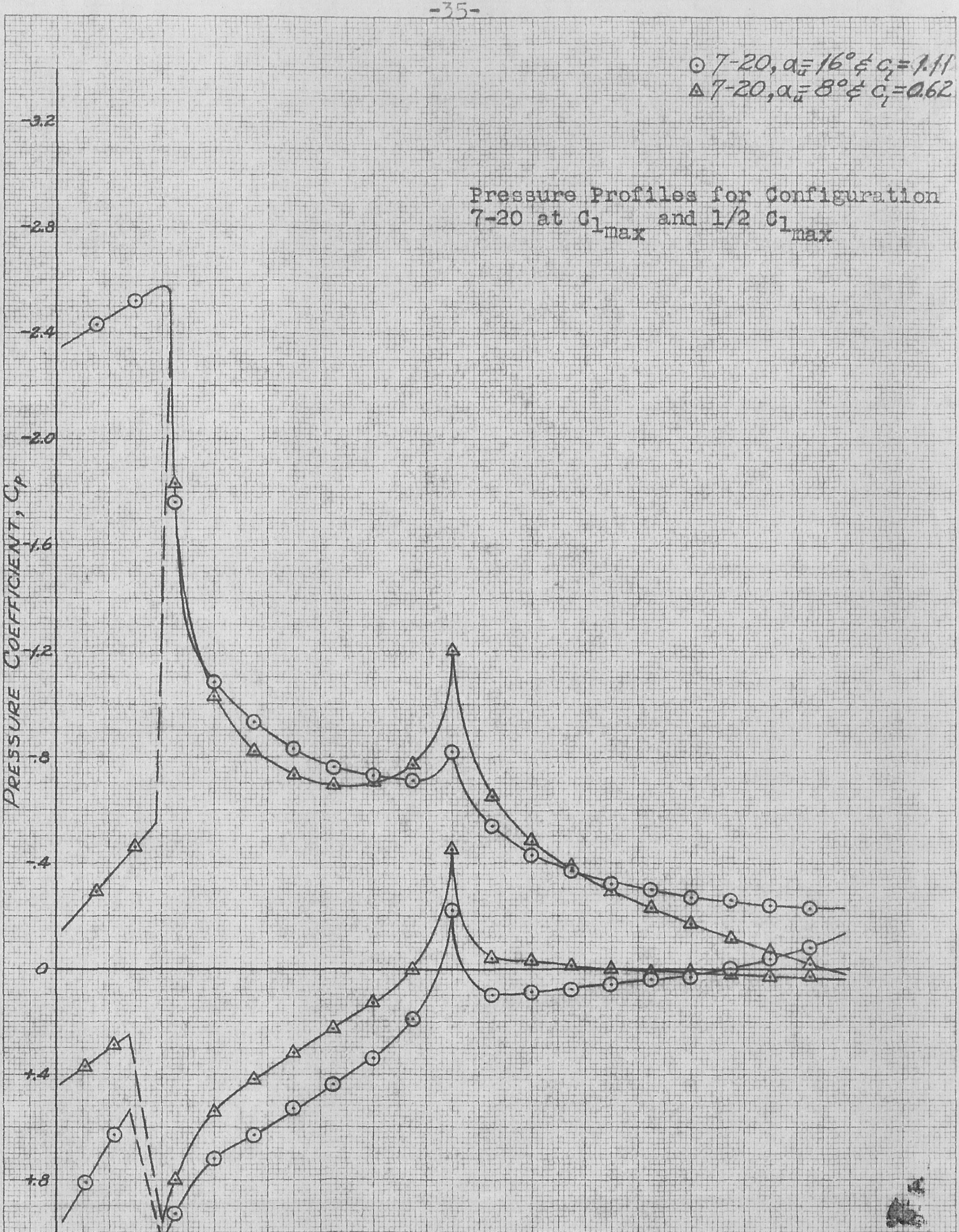
⊙ 7-20, α_u = 16° & c_l = 1.11
△ 7-20, α_u = 8° & c_l = 0.62
Pressure Profiles for Configuration 7-20 at $C_{l_{max}}$ and 1/2 $C_{l_{max}}$
Pressure Coefficient, C_p
-3.2
-2.8
-2.4
-2.0
-1.6
-1.2
-.8
-.4
0
+.4
+.8
+1.2
Chord Stations
0
.1
.2
.3
.4
.5
.6
.7
.8
.9
1.0

Figure 18

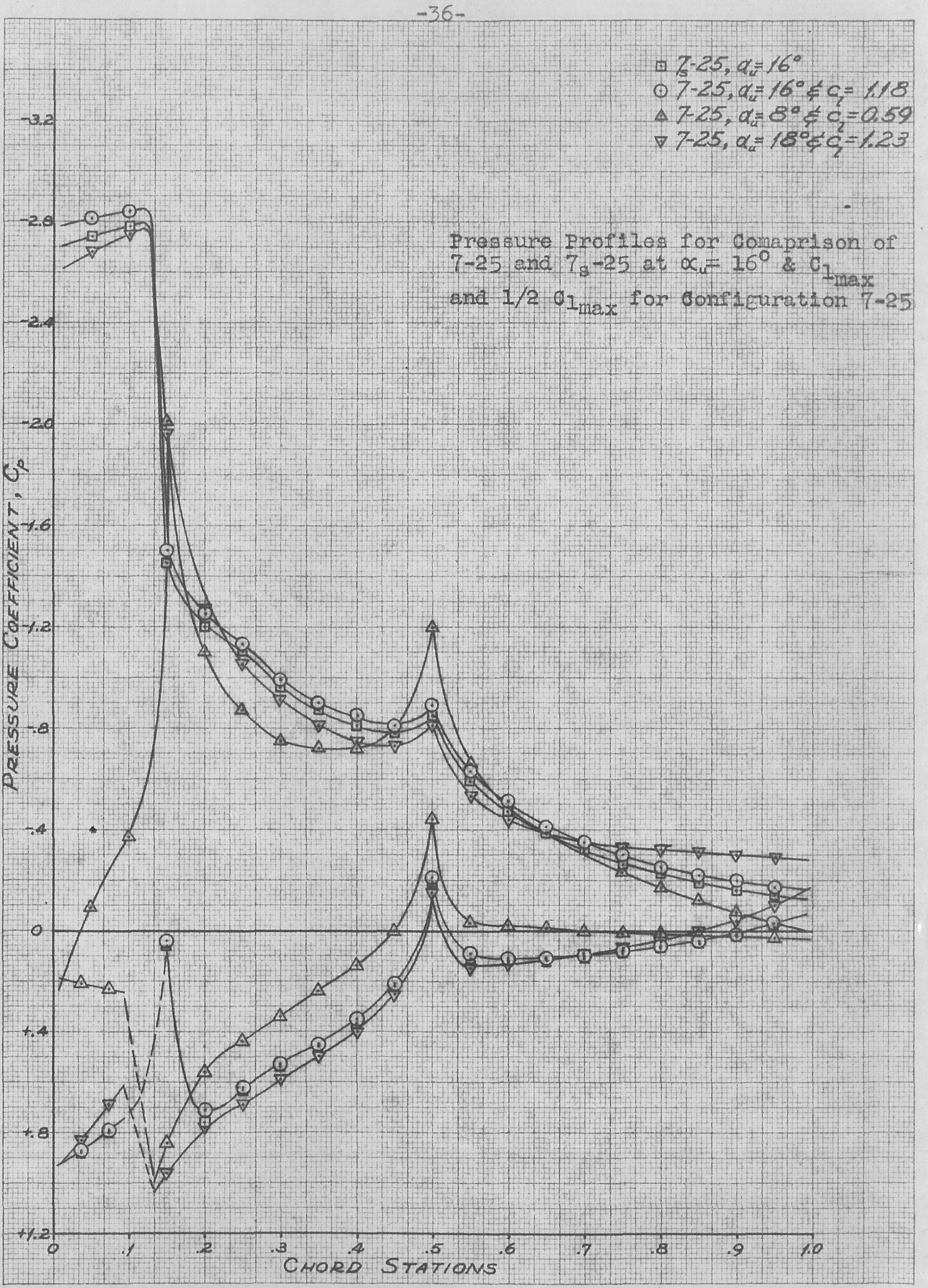
⊡ 7s-25, αu = 16°
⊙ 7-25, αu = 16° & cl = 1.18
△ 7-25, αu = 8° & cl = 0.59
▽ 7-25, αu = 18° & cl = 1.23
Pressure Profiles for Comaprison of 7-25 and 7s-25 at αu = 16° & Cl max and 1/2 Cl max for Configuration 7-25
Pressure Coefficient, Cp
-3.2
-2.8
-2.4
-2.0
-1.6
-1.2
-.8
-.4
0
+.4
+.8
+1.2
Chord Stations
0
.1
.2
.3
.4
.5
.6
.7
.8
.9
1.0

Figure 19

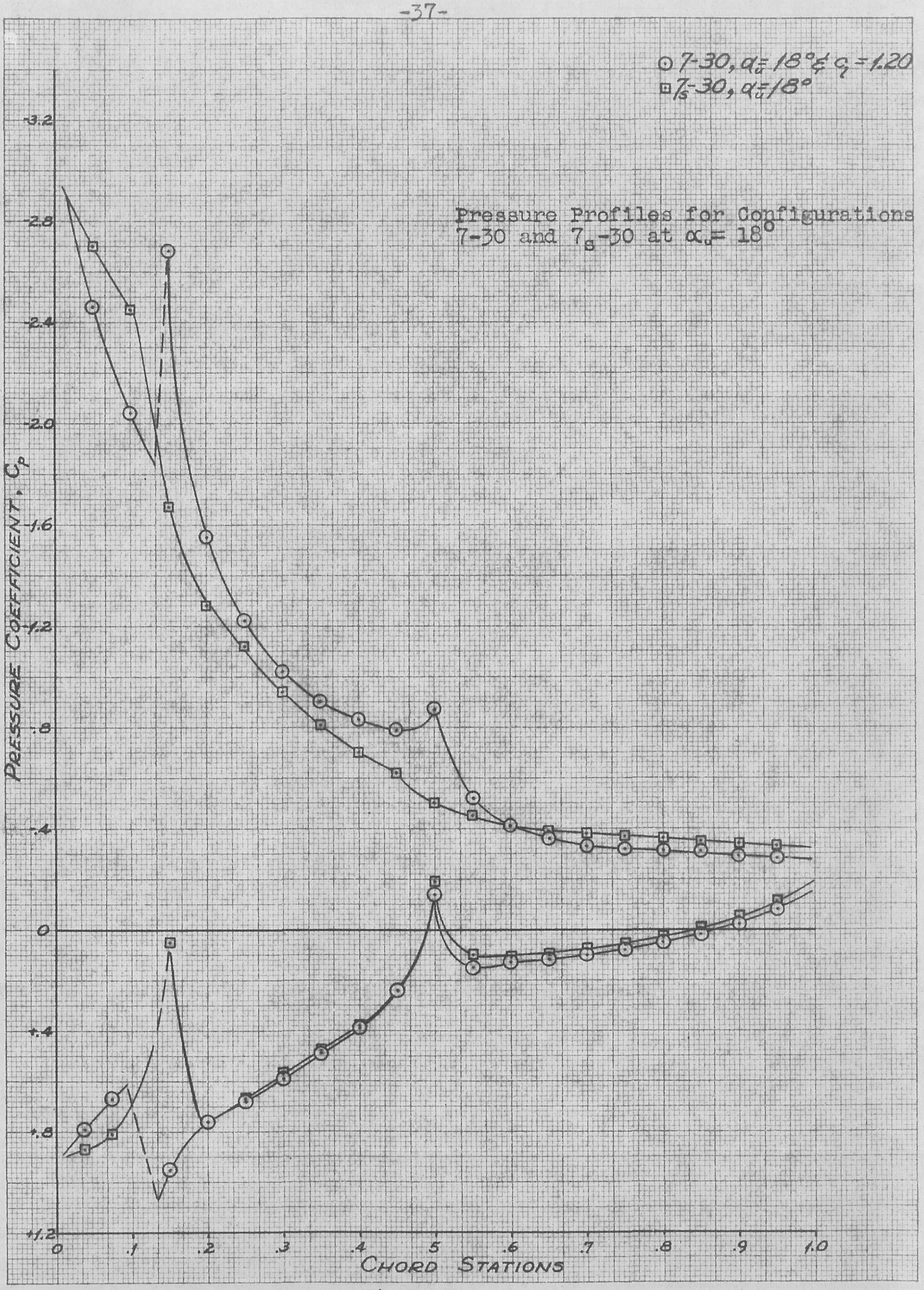
⊙ 7-30, α_u = 18° & c_l = 1.20
⊡ 7_s-30, α_u = 18°
Pressure Profiles for Configurations 7-30 and 7_s-30 at α_u = 18°
Pressure Coefficient, C_p
-3.2
-2.8
-2.4
-2.0
-1.6
-1.2
-.8
-.4
0
+.4
+.8
+1.2
Chord Stations
0
.1
.2
.3
.4
.5
.6
.7
.8
.9
1.0

Figure 20

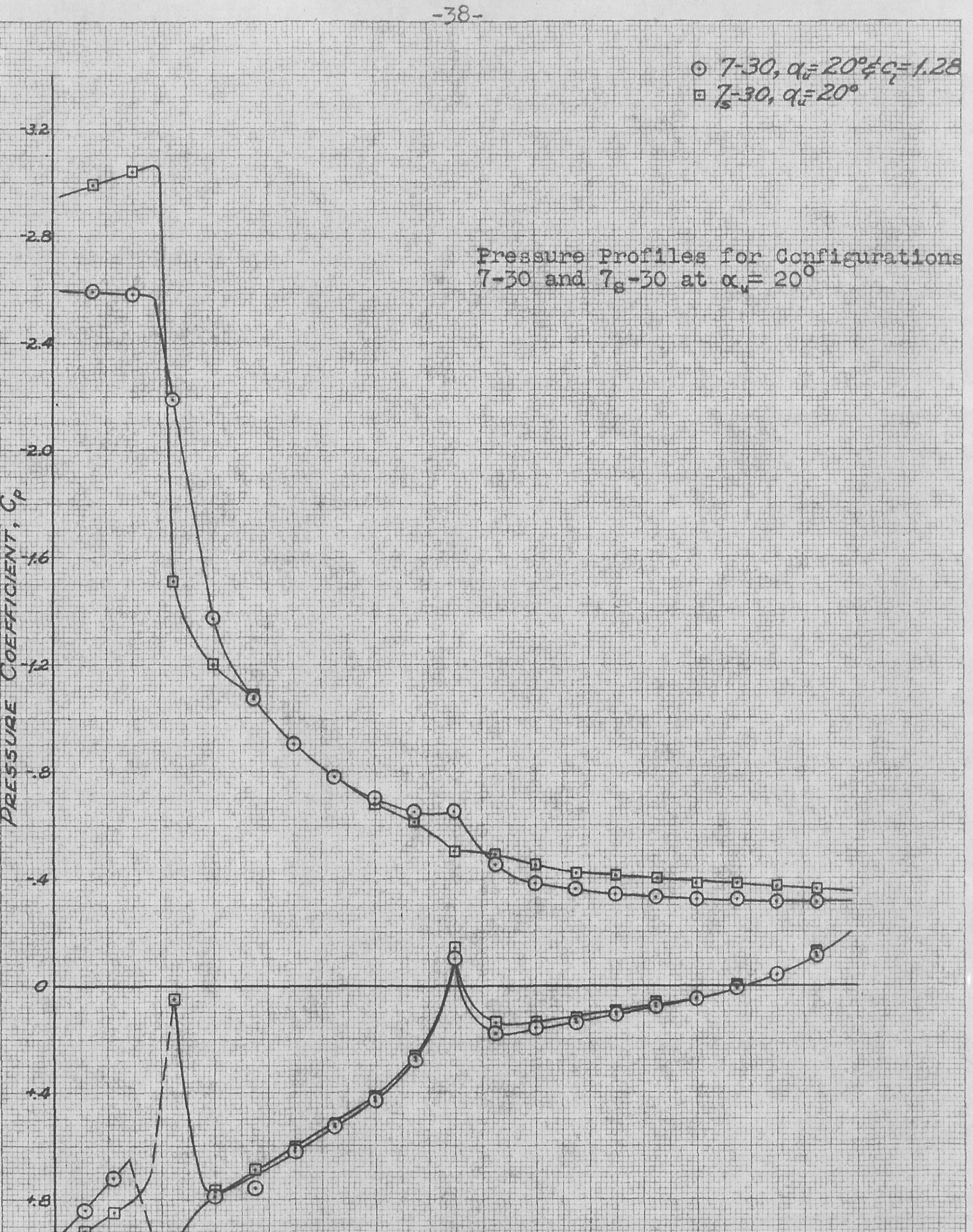

Pressure Profiles for Configurations 7-30 and 7_s-30 at $\alpha_u = 20°$

Figure 21

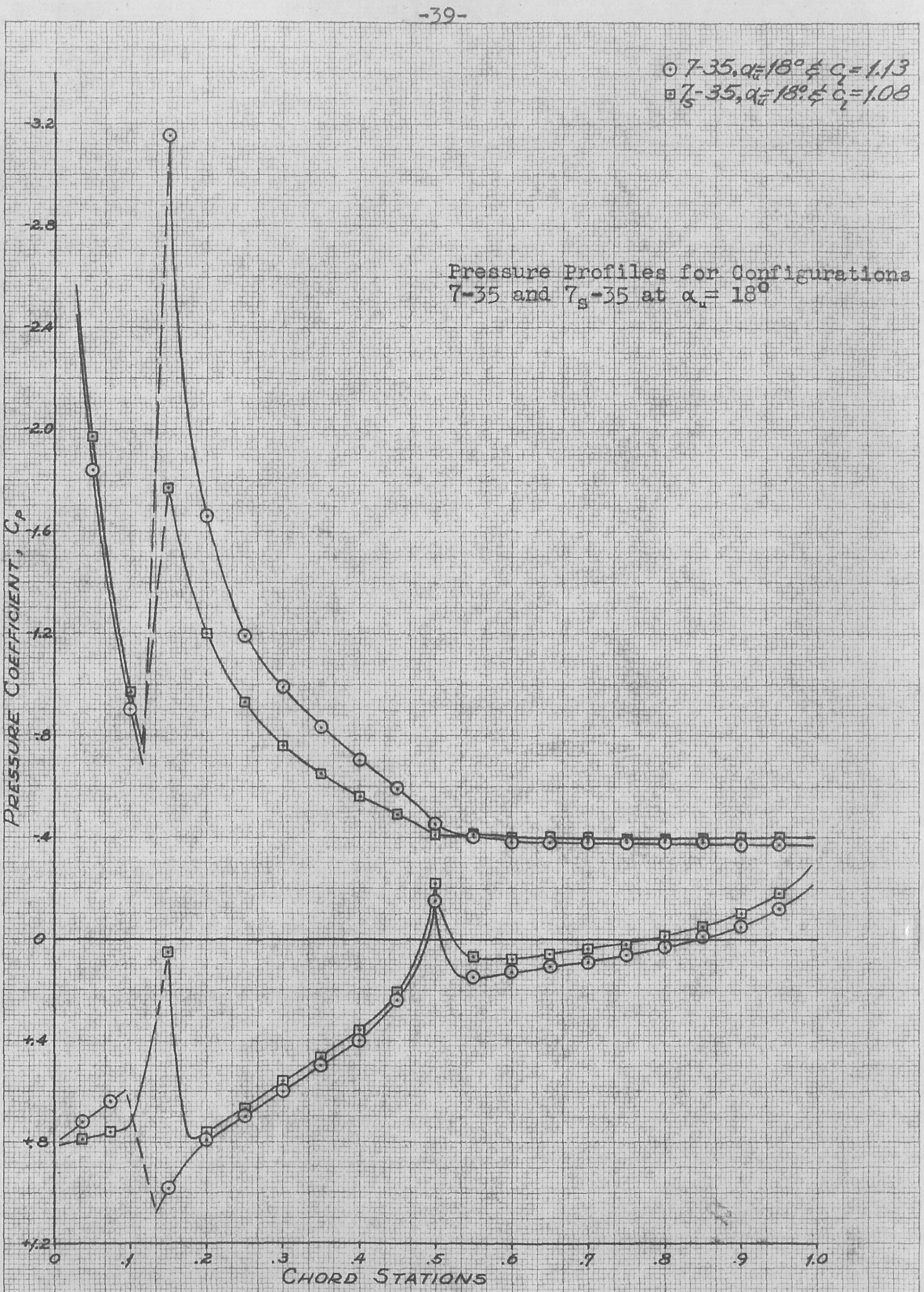
⊙ 7-35, α_u = 18° & C_l = 1.13
⊡ 7_s-35, α_u = 18° & C_l = 1.08
Pressure Profiles for Configurations
7-35 and 7_s-35 at α_u = 18°
PRESSURE COEFFICIENT, C_P
-3.2
-2.8
-2.4
-2.0
-1.6
-1.2
-.8
-.4
0
+.4
+.8
+1.2
0
.1
.2
.3
.4
.5
.6
.7
.8
.9
1.0
CHORD STATIONS

Figure 22

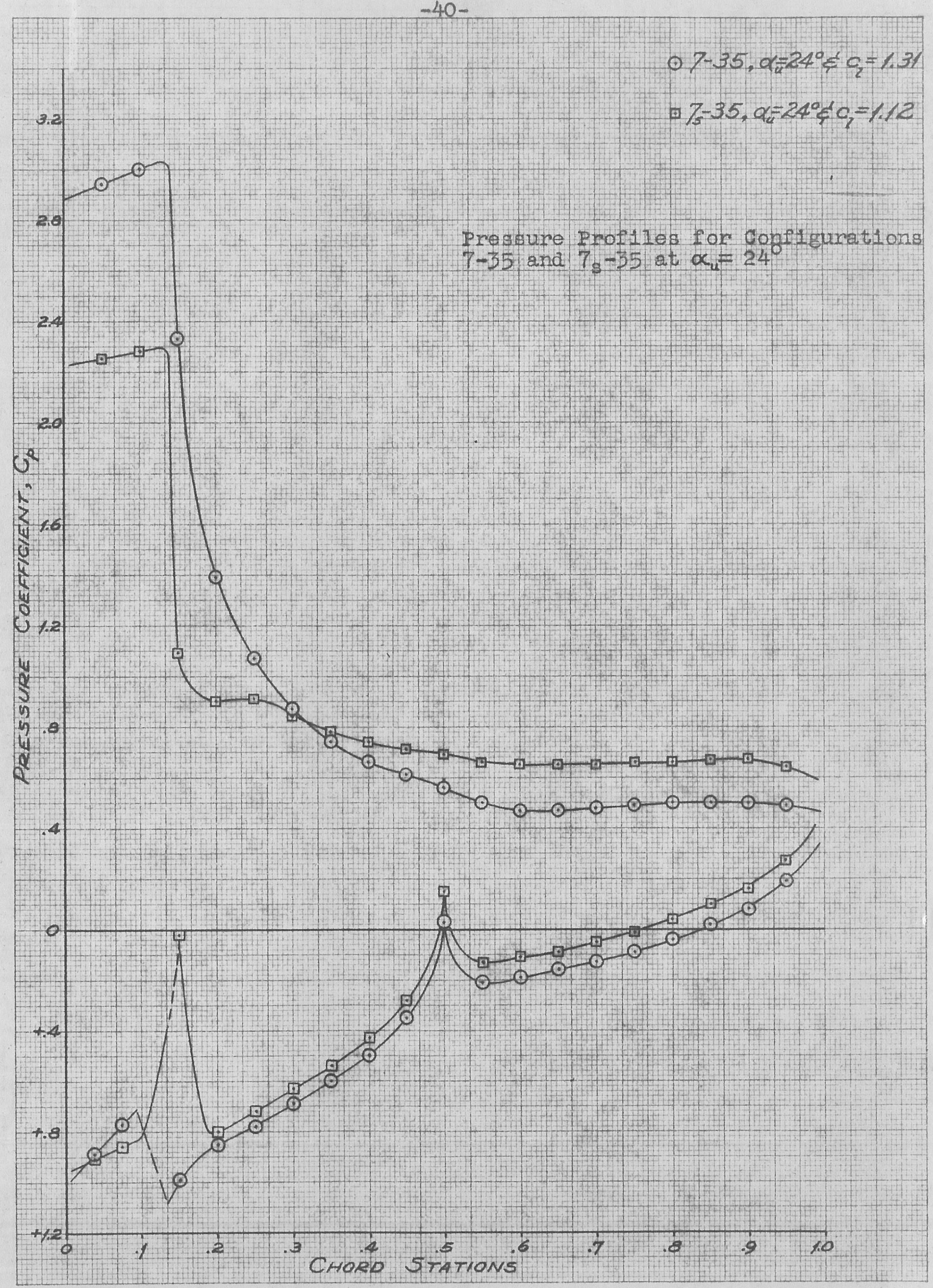
Pressure Profiles for Configurations 7-35 and 7_s-35 at $\alpha_u = 24°$

Figure 23

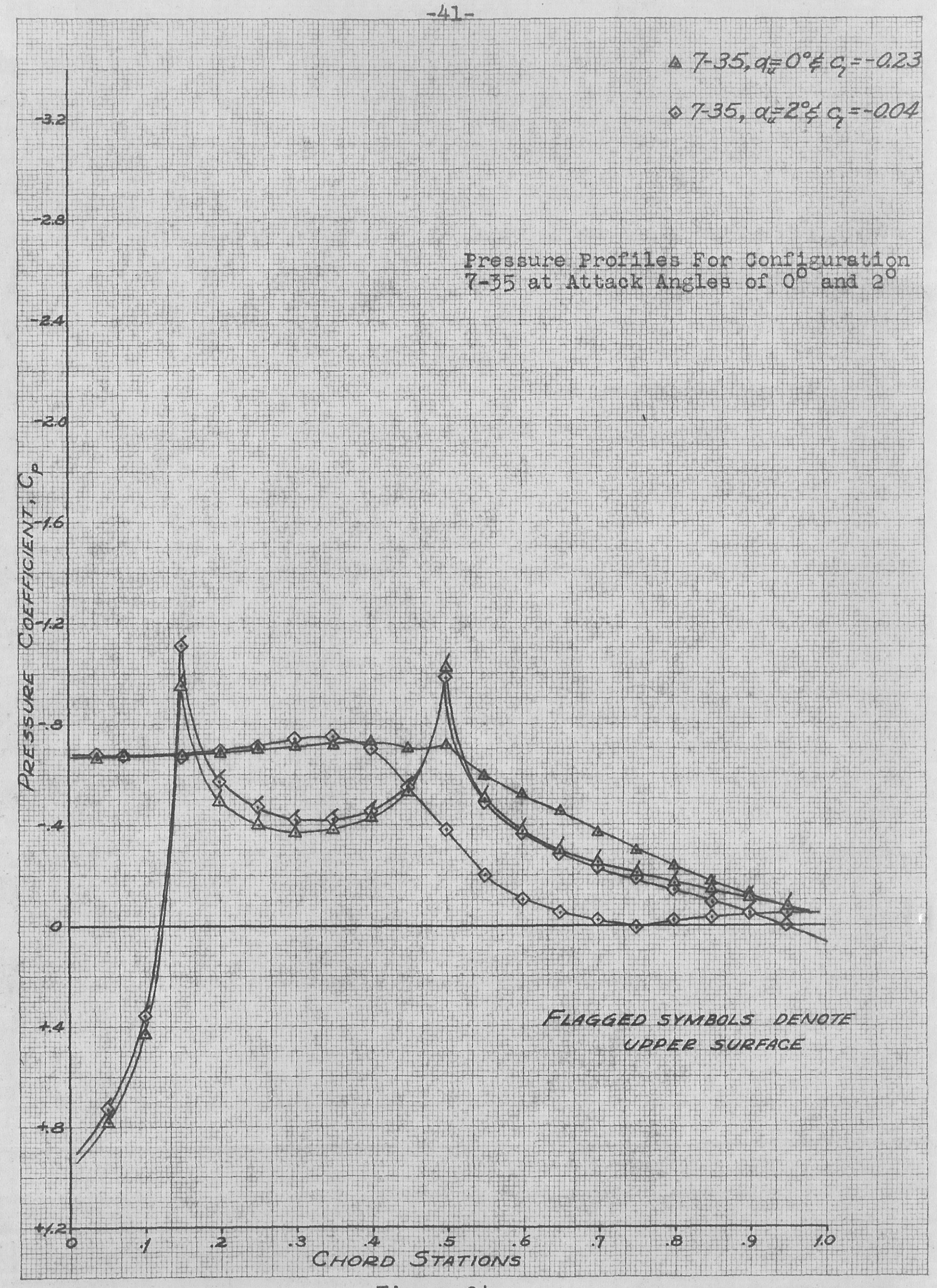
▲ 7-35, α_u=0° & c_l=-0.23
◇ 7-35, α_u=2° & c_l=-0.04
Pressure Profiles For Configuration 7-35 at Attack Angles of 0° and 2°
FLAGGED SYMBOLS DENOTE UPPER SURFACE
PRESSURE COEFFICIENT, C_p
-3.2
-2.8
-2.4
-2.0
-1.6
-1.2
-.8
-.4
0
+.4
+.8
+1.2
CHORD STATIONS
0
.1
.2
.3
.4
.5
.6
.7
.8
.9
1.0

Figure 24

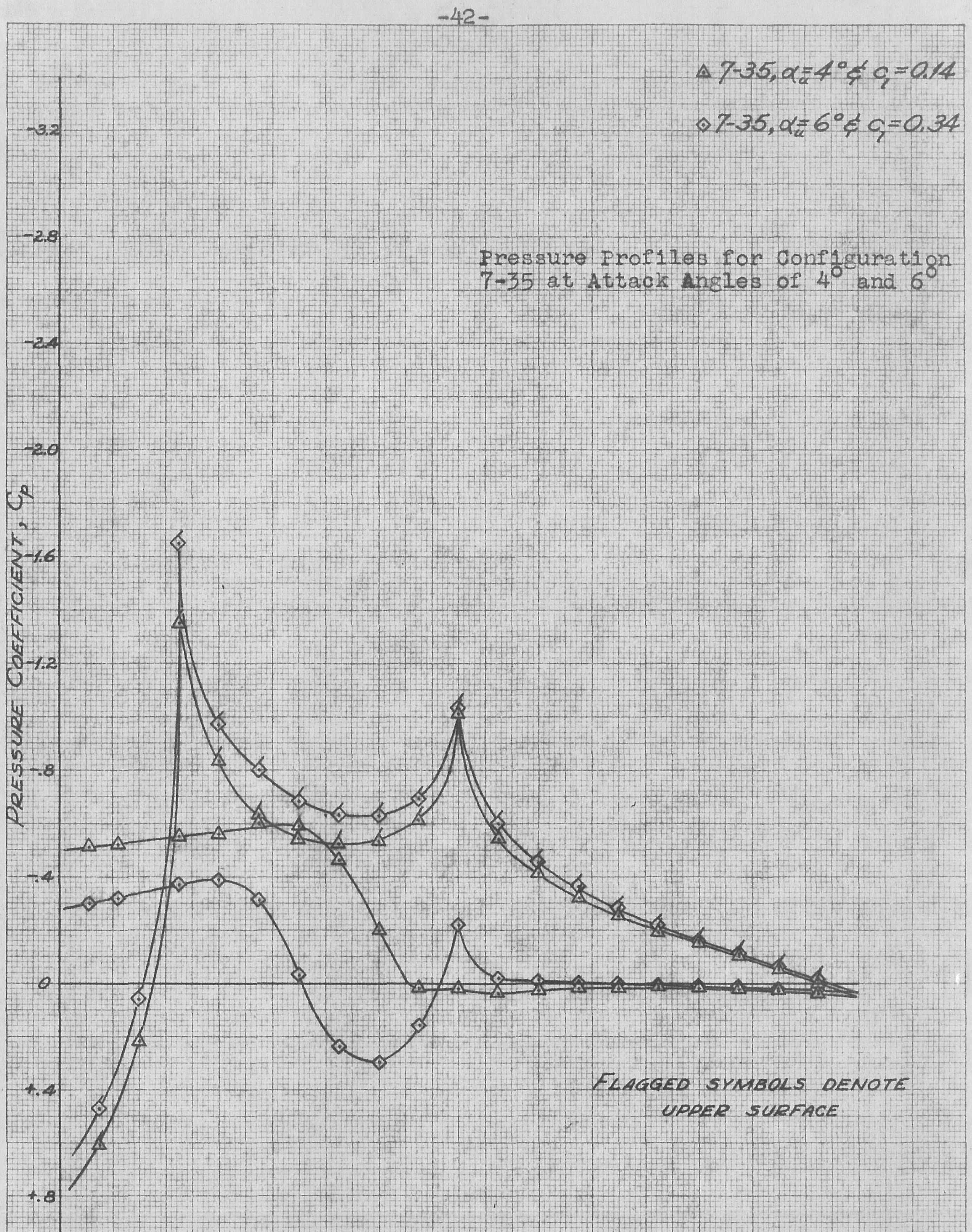

Pressure Profiles for Configuration 7-35 at Attack Angles of 4° and 6°

Figure 25

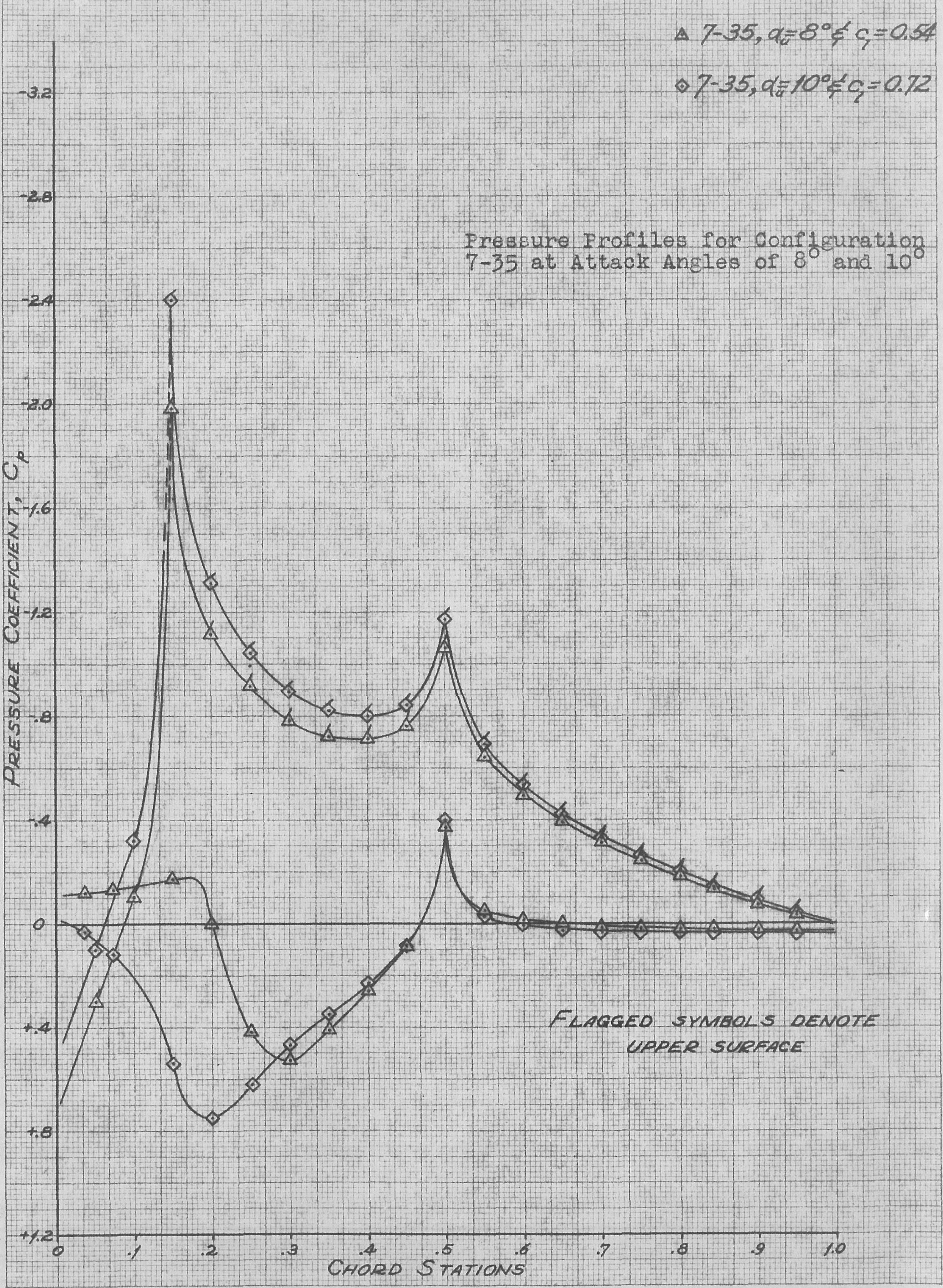

Pressure Profiles for Configuration 7-35 at Attack Angles of 8° and 10°

FLAGGED SYMBOLS DENOTE UPPER SURFACE

Figure 26

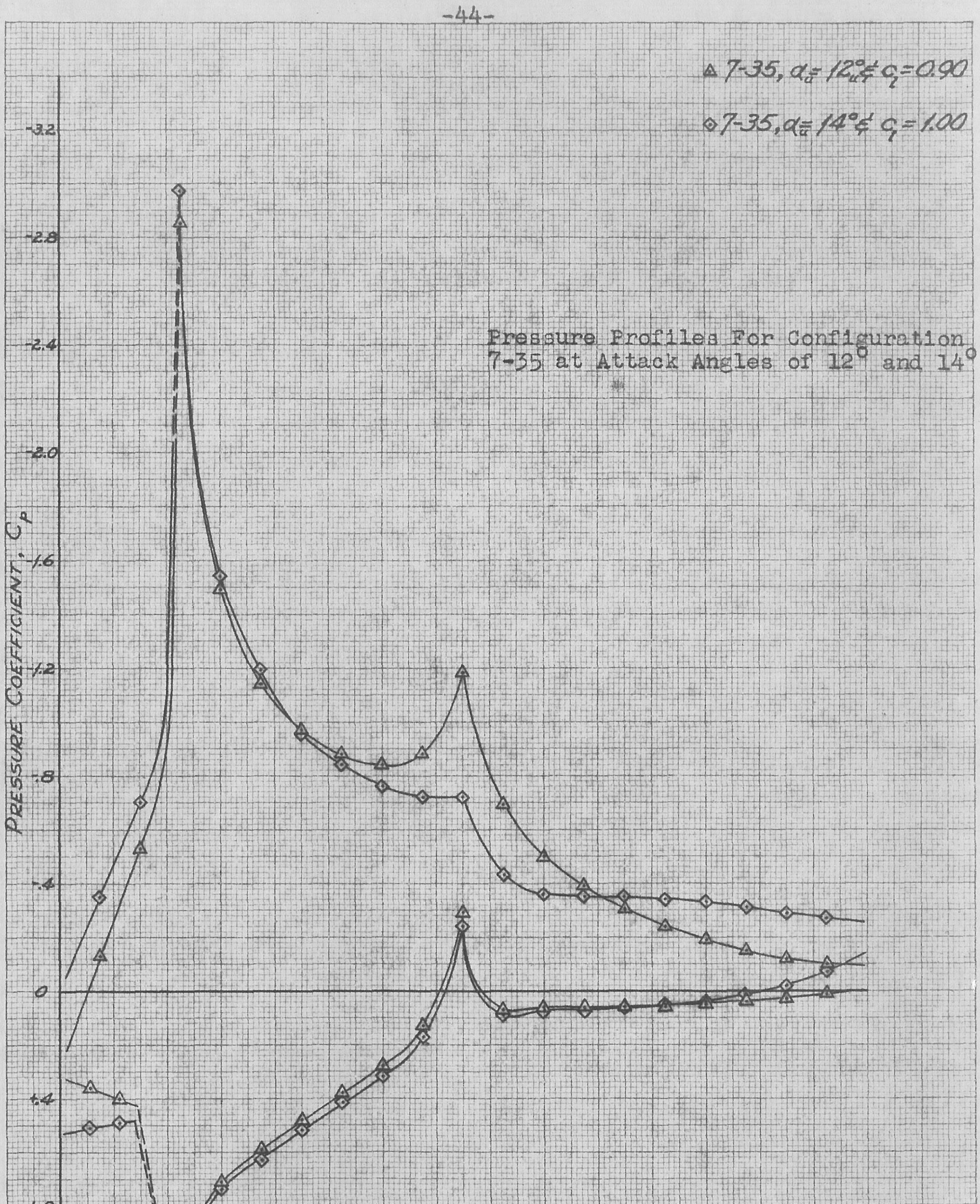

Pressure Profiles For Configuration 7-35 at Attack Angles of 12° and 14°

Figure 27

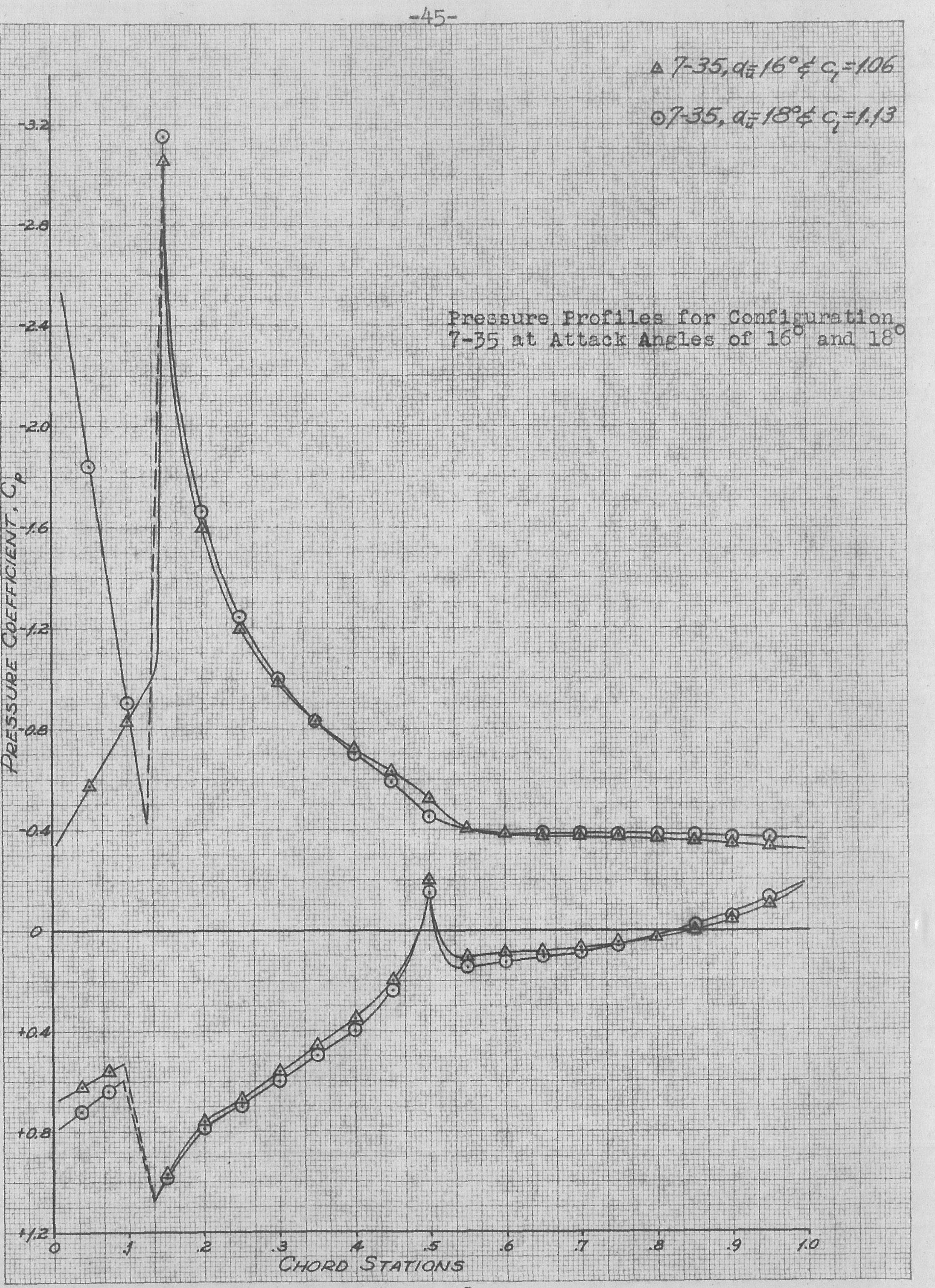

Pressure Profiles for Configuration 7-35 at Attack Angles of 16° and 18°

Figure 28

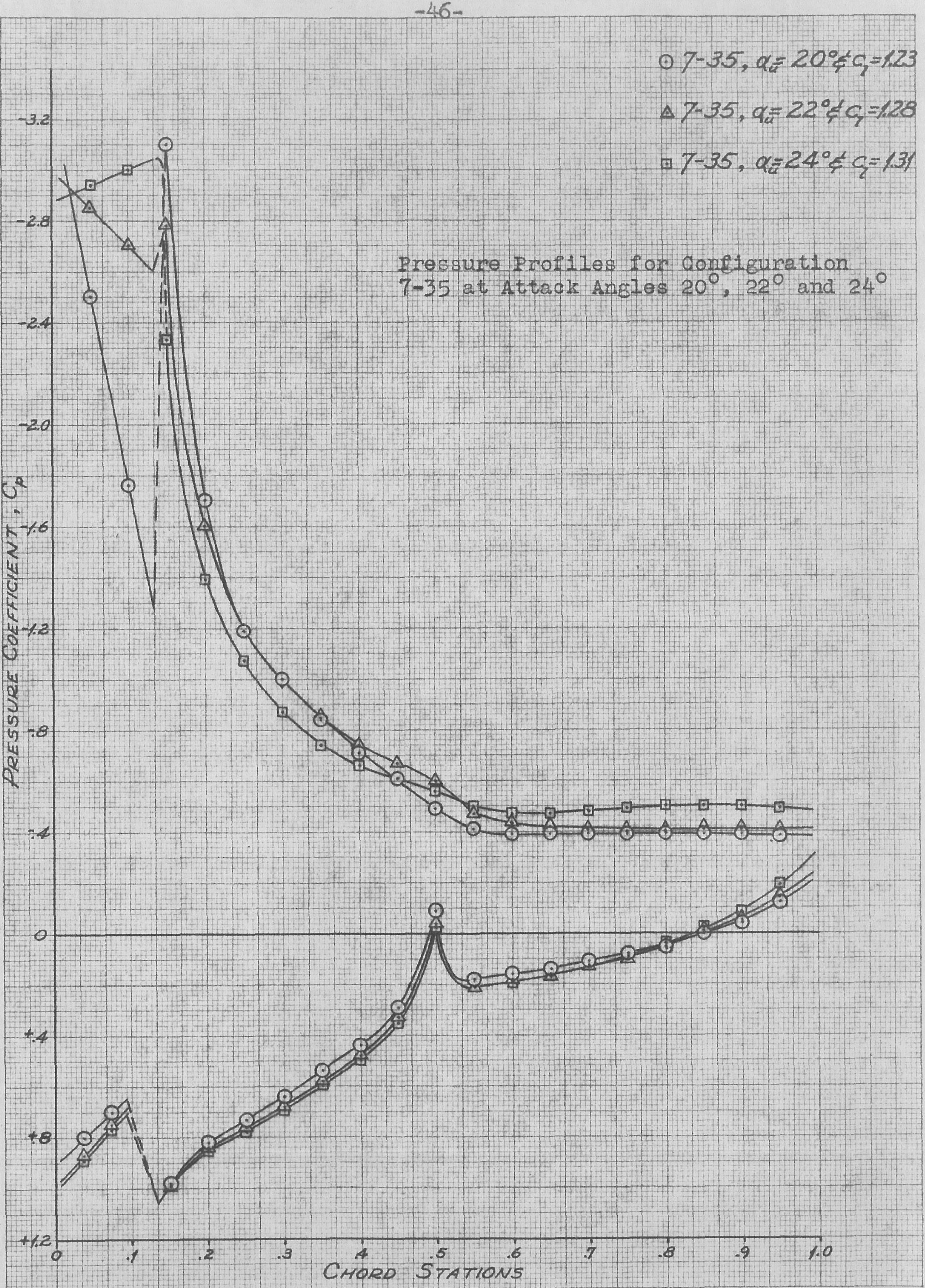

Pressure Profiles for Configuration 7-35 at Attack Angles 20°, 22° and 24°

Figure 29

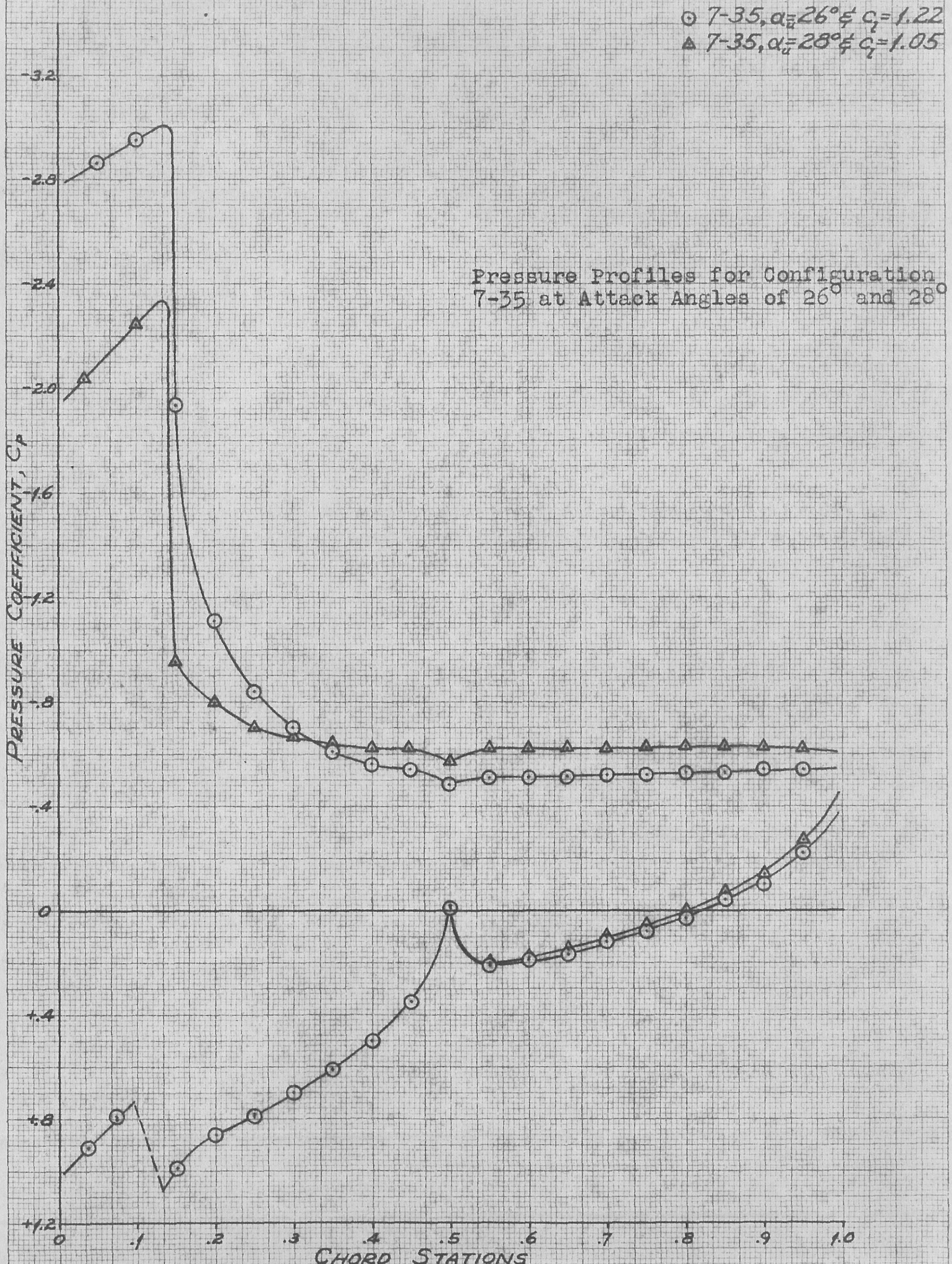
⊙ 7-35, α_u=26° & c_l=1.22
▲ 7-35, α_u=28° & c_l=1.05
Pressure Profiles for Configuration 7-35 at Attack Angles of 26° and 28°
PRESSURE COEFFICIENT, C_p
-3.2
-2.8
-2.4
-2.0
-1.6
-1.2
-.8
-.4
0
+.4
+.8
+1.2
0
.1
.2
.3
.4
.5
.6
.7
.8
.9
1.0
CHORD STATIONS

Figure 30

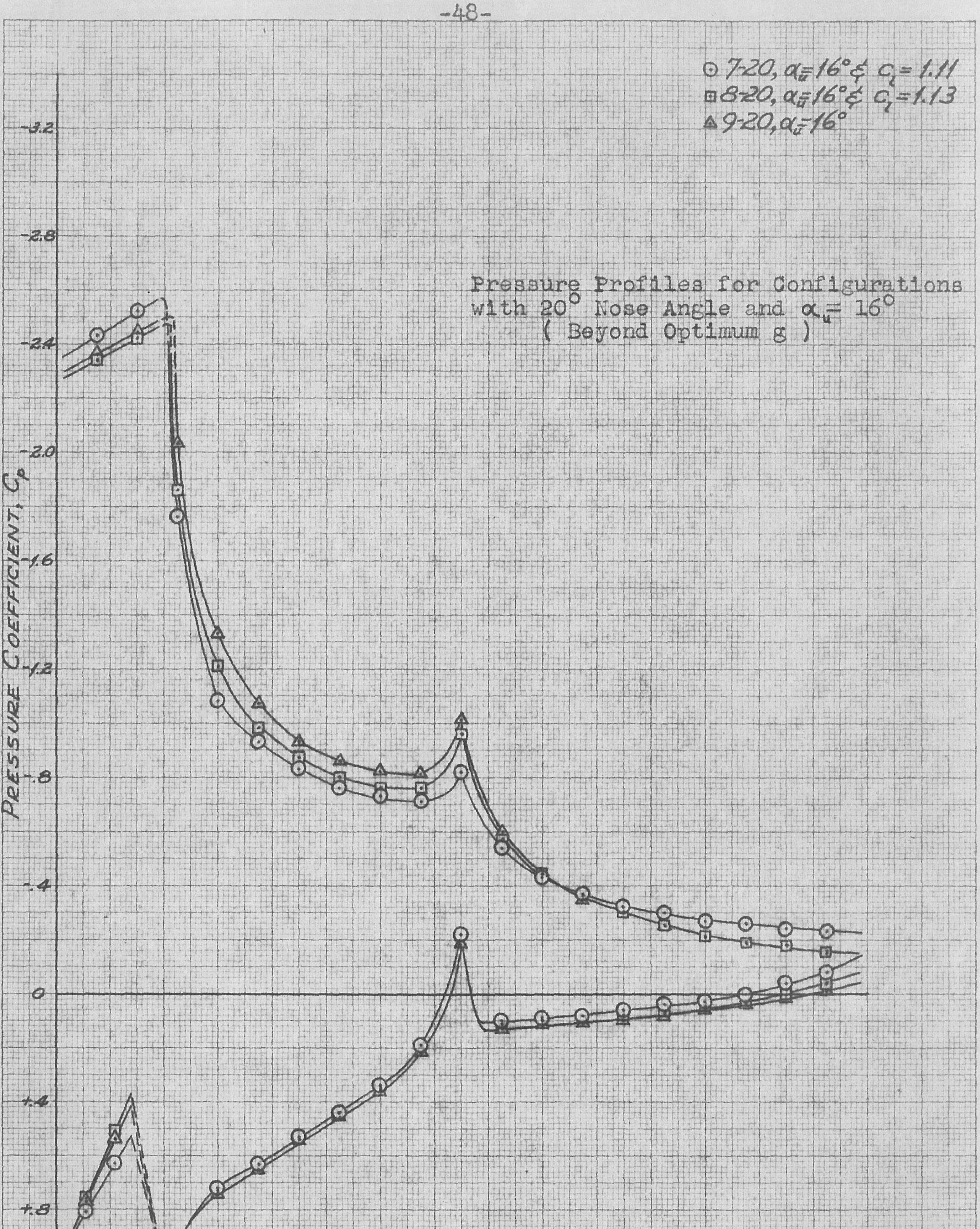
⊙ 7-20, α_u=16° & C_l = 1.11
⊡ 8-20, α_u=16° & C_l = 1.13
▲ 9-20, α_u=16°
Pressure Profiles for Configurations
with 20° Nose Angle and α_u= 16°
(Beyond Optimum g)
PRESSURE COEFFICIENT, C_p
-3.2
-2.8
-2.4
-2.0
-1.6
-1.2
-.8
-.4
0
+.4
+.8
+1.2
0
.1
.2
.3
.4
.5
.6
.7
.8
.9
1.0
CHORD STATIONS

Figure 31

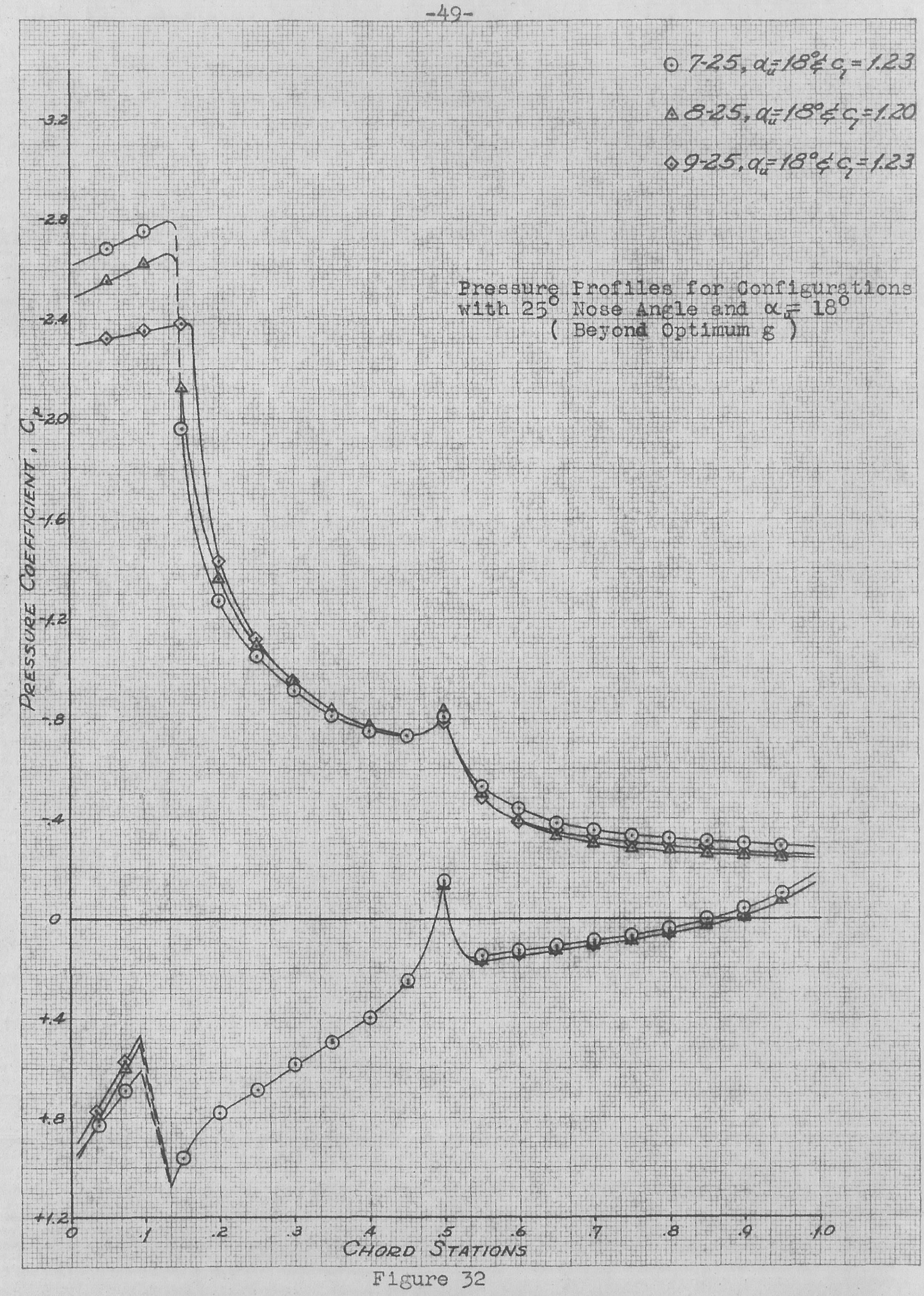
⊙ 7-25, α_u = 18° & c_l = 1.23
△ 8-25, α_u = 18° & c_l = 1.20
◇ 9-25, α_u = 18° & c_l = 1.23
Pressure Profiles for Configurations with 25° Nose Angle and α_u = 18°
(Beyond Optimum g)
Pressure Coefficient, C_p
-3.2
-2.8
-2.4
-2.0
-1.6
-1.2
-.8
-.4
0
+.4
+.8
+1.2
0
.1
.2
.3
.4
.5
.6
.7
.8
.9
1.0
Chord Stations

Figure 32

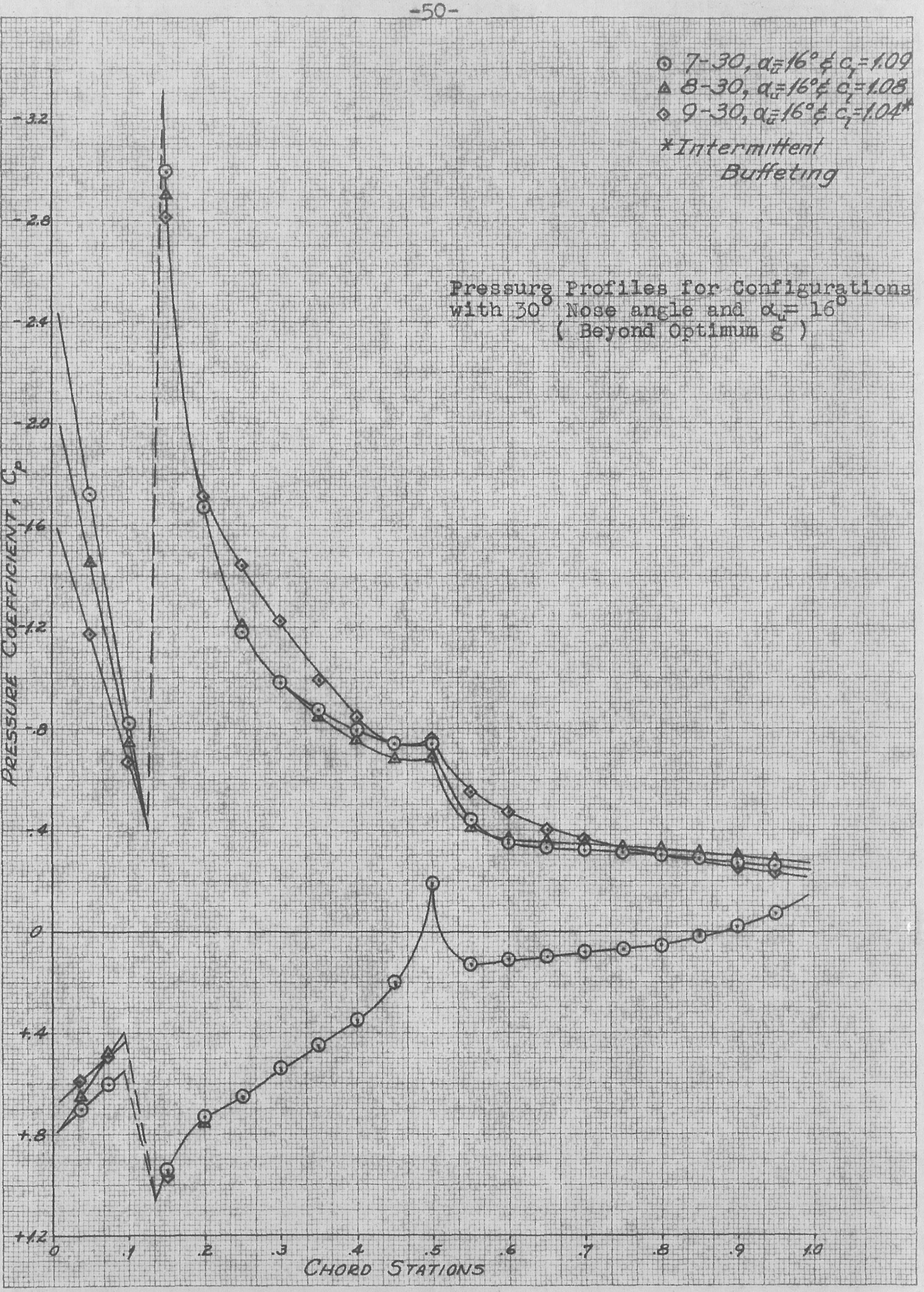

Pressure Profiles for Configurations with 30° Nose angle and $\alpha_u = 16°$ (Beyond Optimum g)

Figure 33

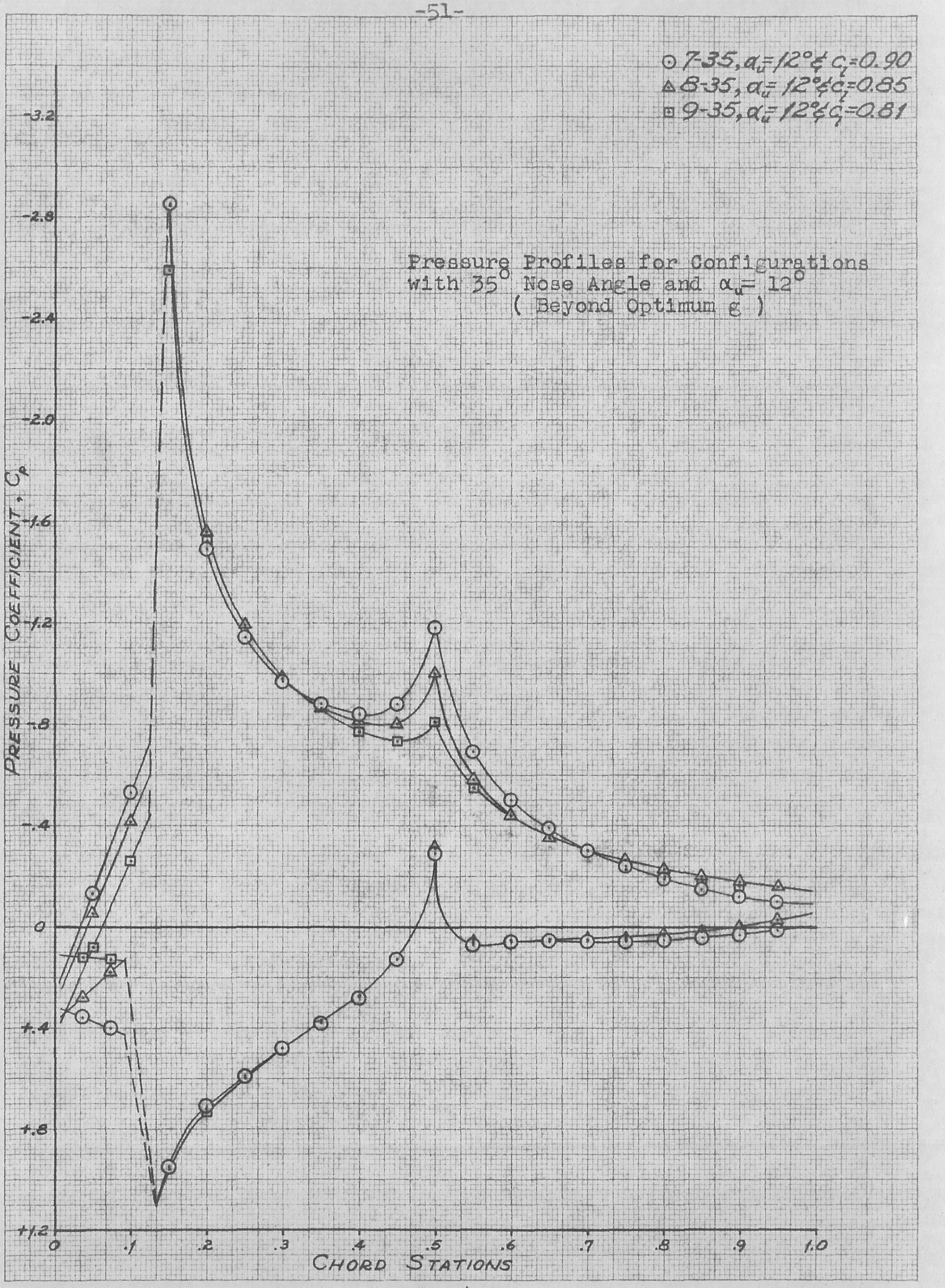

Pressure Profiles for Configurations with 35° Nose Angle and $\alpha_u = 12°$ (Beyond Optimum g)

Figure 34

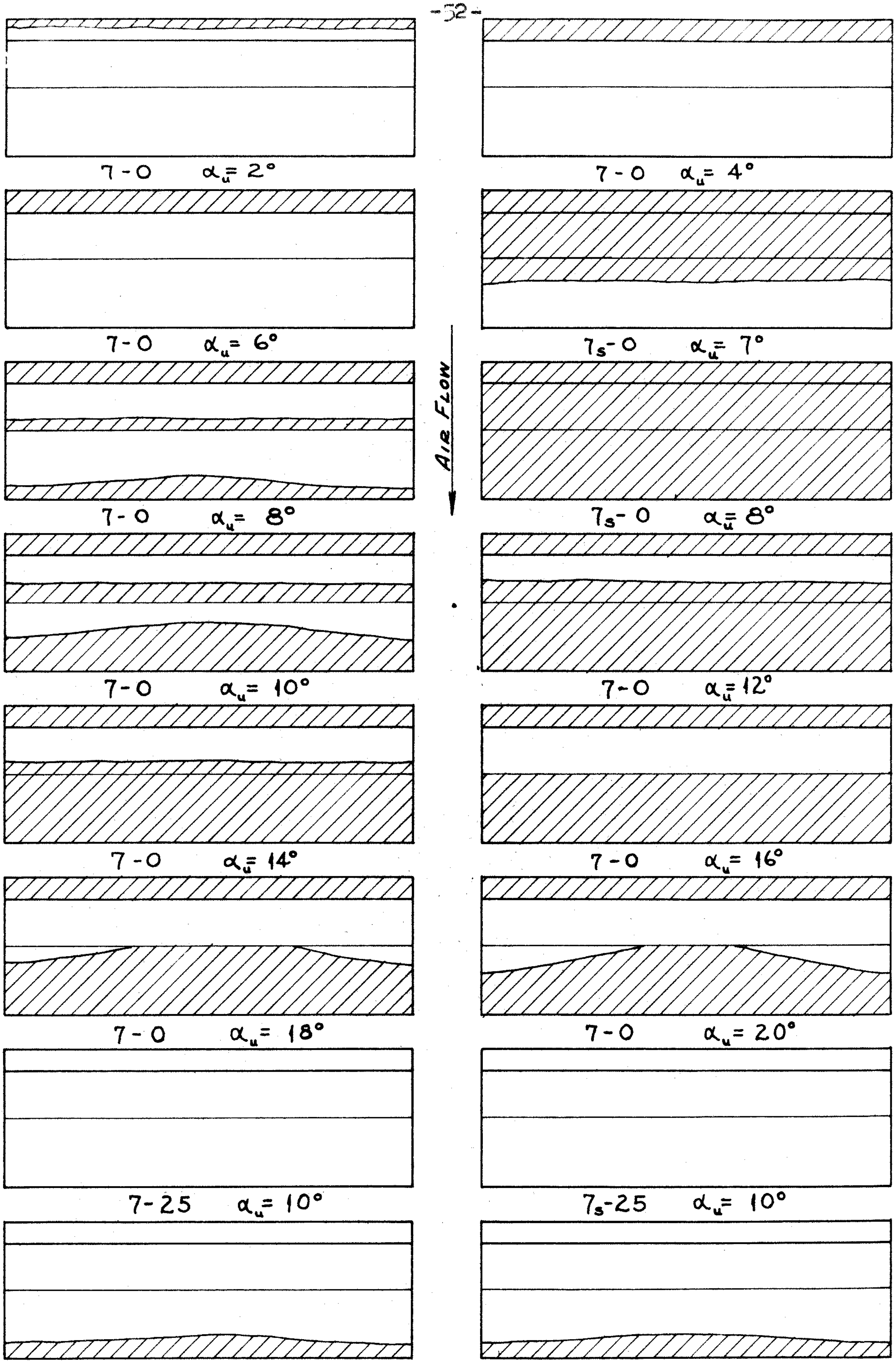

7-0 $\alpha_u = 2°$

7-0 $\alpha_u = 4°$

7-0 $\alpha_u = 6°$

7_s-0 $\alpha_u = 7°$

7-0 $\alpha_u = 8°$

7_s-0 $\alpha_u = 8°$

7-0 $\alpha_u = 10°$

7-0 $\alpha_u = 12°$

7-0 $\alpha_u = 14°$

7-0 $\alpha_u = 16°$

7-0 $\alpha_u = 18°$

7-0 $\alpha_u = 20°$

7-25 $\alpha_u = 10°$

7_s-25 $\alpha_u = 10°$

7-25 $\alpha_u = 12°$

7_s-25 $\alpha_u = 12°$

<u>Tuft Pattern Sketches</u> Figure 35

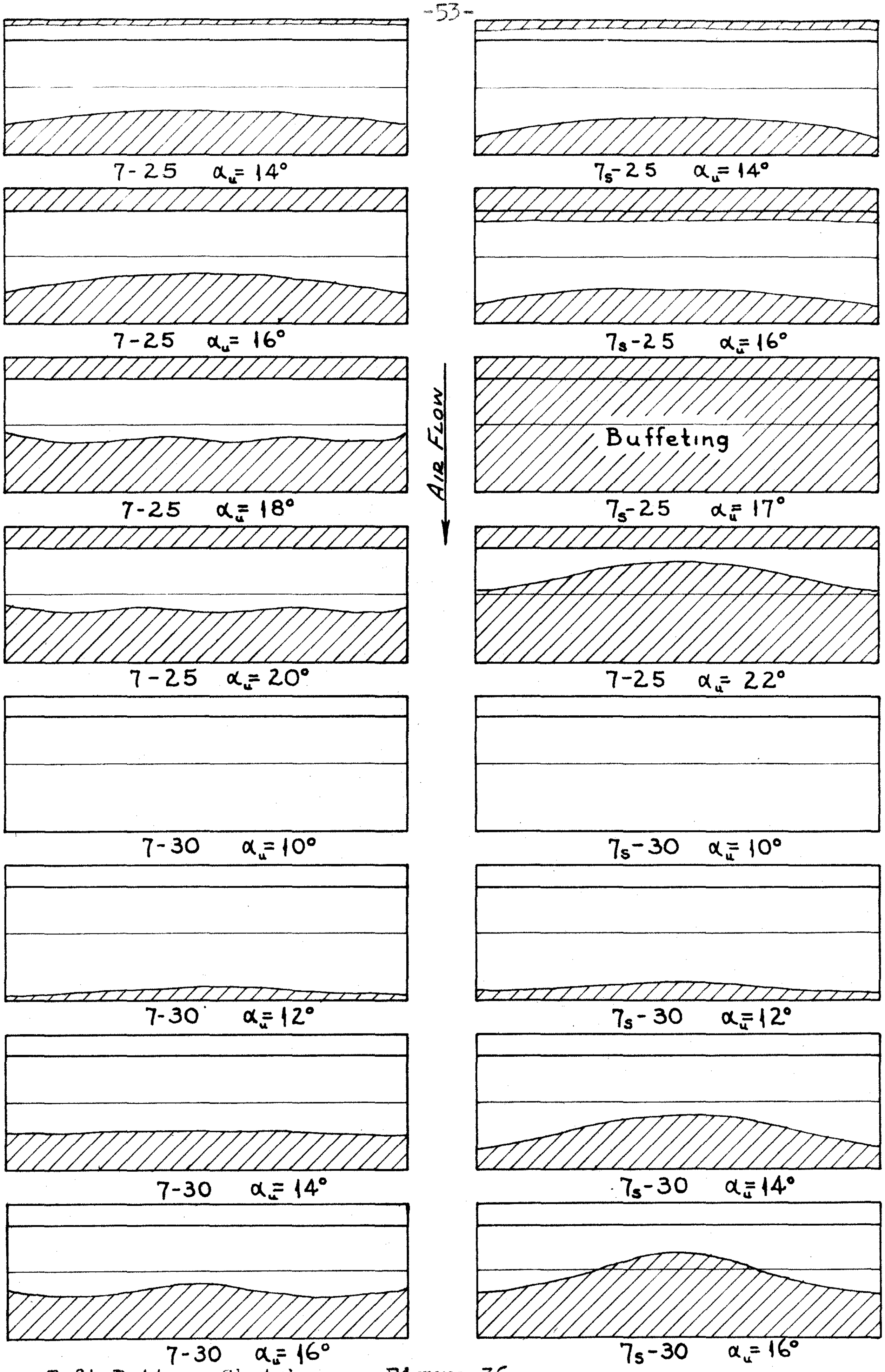

Tuft Pattern Sketches Figure 36

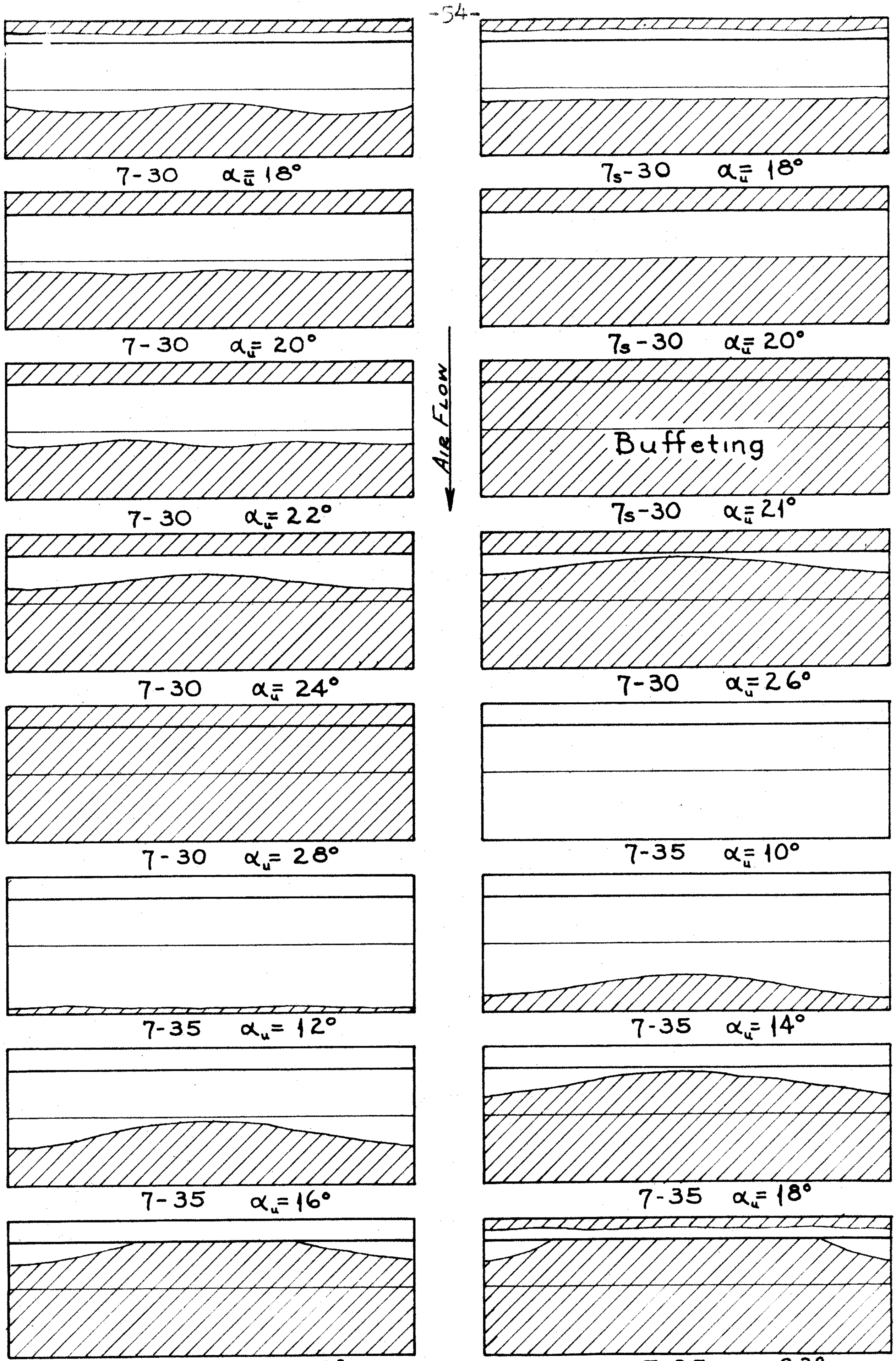

7-30 $\alpha_u = 18^\circ$

7s-30 $\alpha_u = 18^\circ$

7-30 $\alpha_u = 20^\circ$

7s-30 $\alpha_u = 20^\circ$

7-30 $\alpha_u = 22^\circ$

7s-30 $\alpha_u = 21^\circ$

7-30 $\alpha_u = 24^\circ$

7-30 $\alpha_u = 26^\circ$

7-30 $\alpha_u = 28^\circ$

7-35 $\alpha_u = 10^\circ$

7-35 $\alpha_u = 12^\circ$

7-35 $\alpha_u = 14^\circ$

7-35 $\alpha_u = 16^\circ$

7-35 $\alpha_u = 18^\circ$

7-35 $\alpha_u = 20^\circ$

7-35 $\alpha_u = 22^\circ$

Tuft Pattern Sketches Figure 37

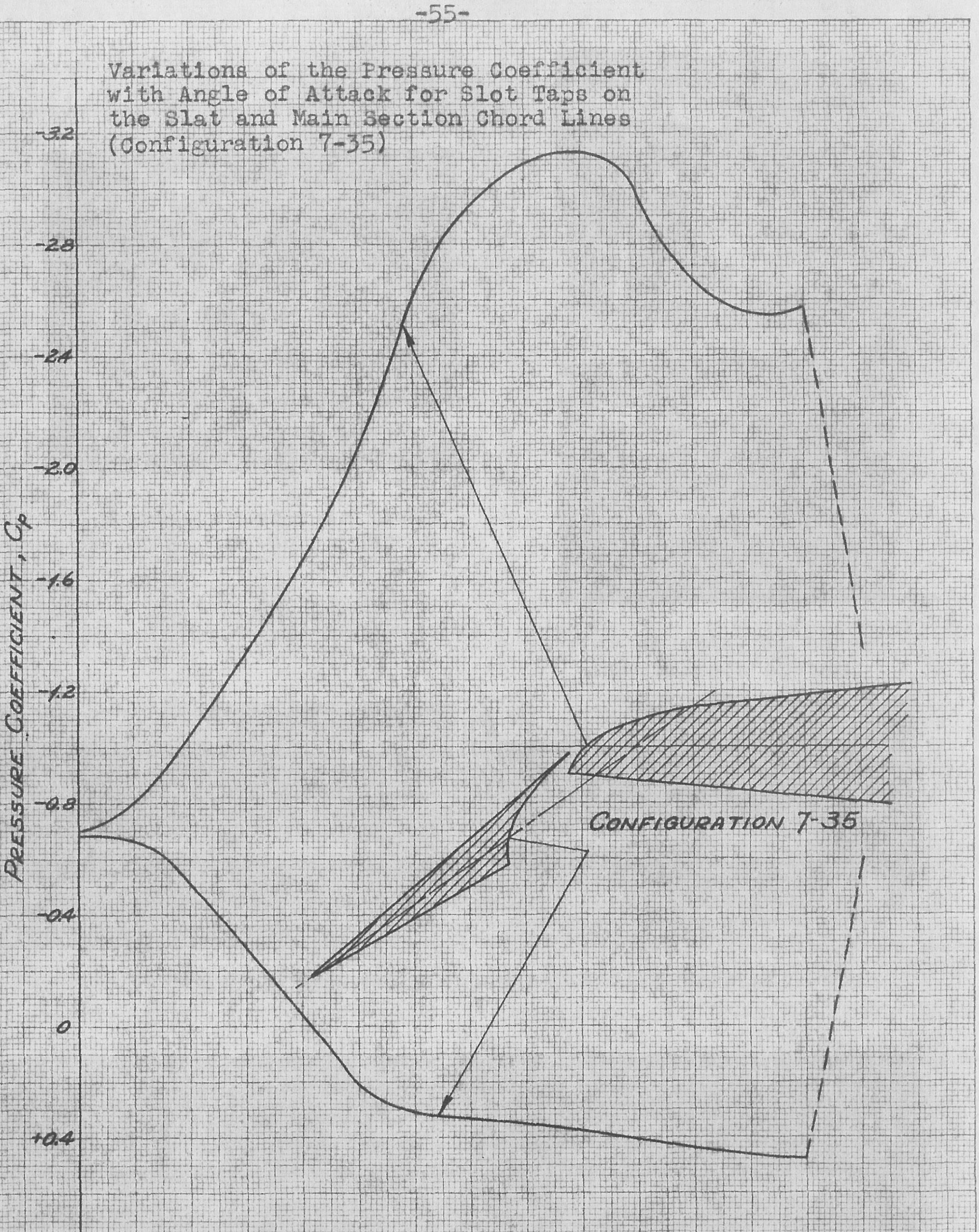

Variations of the Pressure Coefficient with Angle of Attack for Slot Taps on the Slat and Main Section Chord Lines (Configuration 7-35)

Figure 38

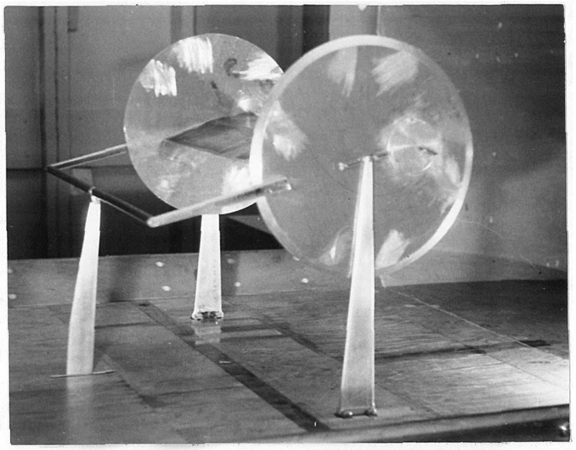

Three-quarter rear view
of model in tunnel throat

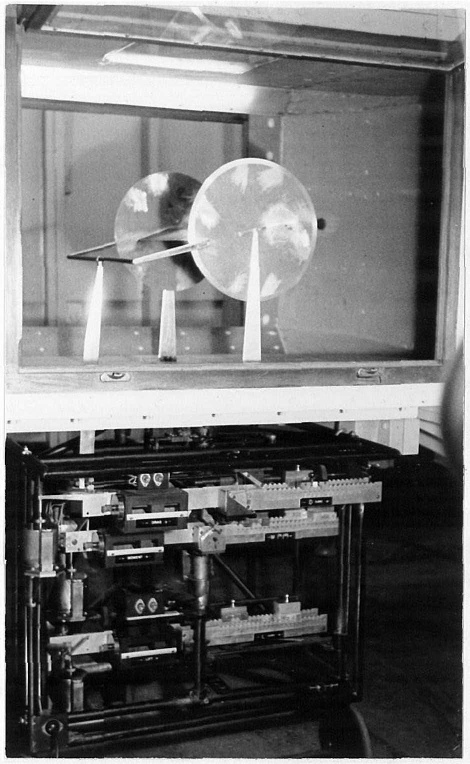

View of model in tunnel
and balance sustem

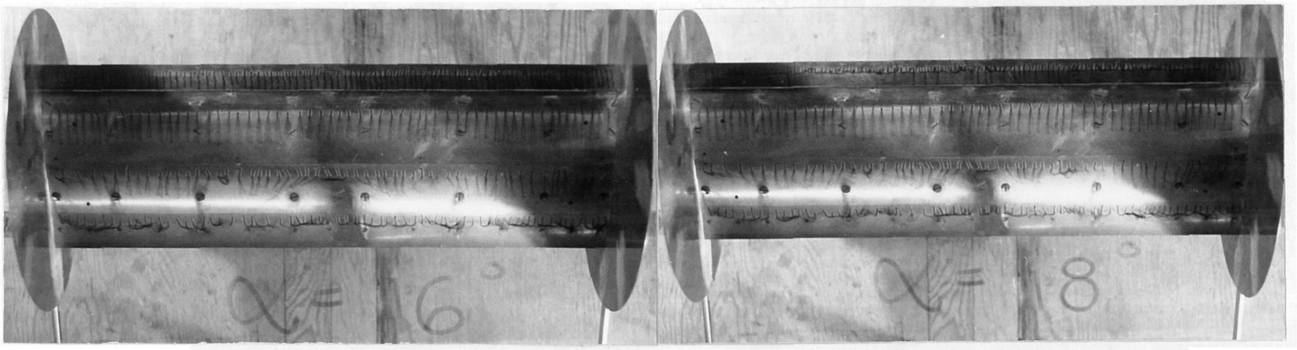

Photographs typical of nose separation progression

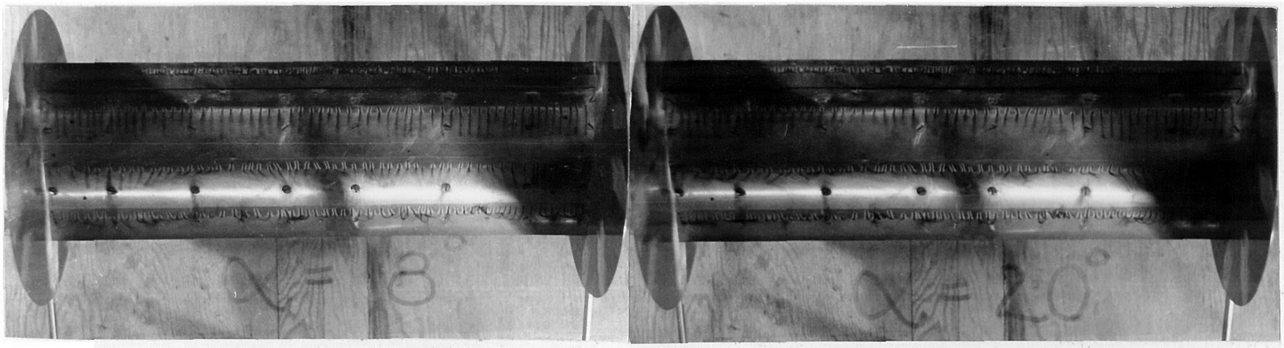

Photographs typical of trailing-edge separation progression

Model and Tuft Photographs

APPENDIX I

DESCRIPTION OF THE MERRILL TUNNEL

The Merrill Tunnel at the California Institute of Technology is a closed circuit type approximately 110 ft. long with a 32 by 45 in. rectangular test section and 6:1 contraction ratio. Power is supplied by a 75 H.P. constant speed electric motor driving a specially designed three-bladed propeller. A velocity range of 0 to 180 mph. at the test section is provided by the electric prop pitch control.

A temporary three force component manual balance system was used for this test program (p. 56). The force limits of the balance were 100 lbs. of lift, 50 lbs. of drag and 125 in.-lbs. of pitching moment. They were beam balances with flexure type pivots throughout and contact point neon lamp balance indicators. Variable dashpot damping was provided on the beams to reduce vibrational interference. Repeatability of measured forces indicated the following force accuracy throughout the load range:

Lift ± 0.01 lb.
Drag ± 0.01 lb.
Pitching Moment ± 0.03 in.-lb.

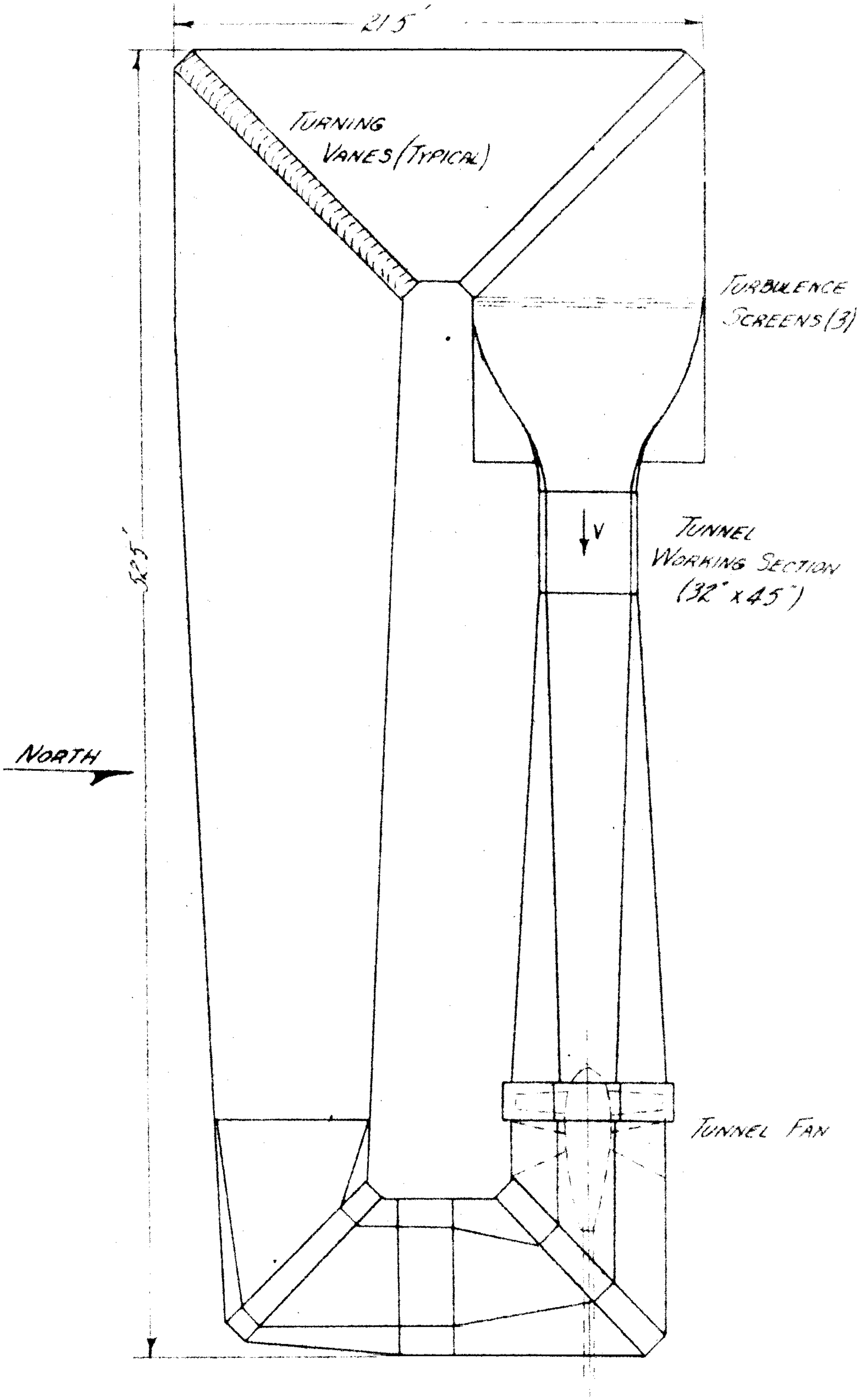

PLANVIEW OF THE
MERRILL WIND TUNNEL

APPENDIX II

SLOT GAP CORRELATION

Since the curvature of the main section nose required radial translation of the slat for constant gap with increased nose deflection, the gap of a given configuration was a function of this curvature. The slat translation number, b, designated the number of half percent chord translations from the original profile position through which the slat had been moved before it was rotated about the 15% chord point to the desired nose angle. Thus the notation of the configurations as b-a meant that the slat had been translated b/2 percent of the chord radially and rotated downward through a degrees from its original position as part of the basic wedge airfoil section. This method of location for the slat required a relationship between the slot gap and the radial translations for the various nose angles used in the investigation; Figure 39 presents the curves of this relationship.

Appendix II
Relationship between Slot Gap g and Slat Translation b for Various Nose Angles a; Configurations b-a